

Shear-wave velocity structure of the Blanco oceanic transform fault zone

Nicholas Irabor Adimah,¹ Yen Joe Tan¹ and Joshua Berryman Russell^{1,2}

¹Department of Earth and Environmental Sciences, The Chinese University of Hong Kong, Hong Kong S.A.R. 0000, China.

E-mails: nickydof@gmail.com; yjtan@cuhk.edu.hk

²Department of Earth and Environmental Sciences, College of Arts and Sciences, Syracuse University, Syracuse, New York 13244, United States

Accepted 2024 September 2. Received 2024 August 14; in original form 2024 April 29

SUMMARY

Oceanic transform faults (OTFs) facilitate hydrothermal circulation which can modify the fault zone materials and affect their rheological evolution. However, the depth extent and variability of fluid infiltration, degree of mineral alteration and their relationship with earthquake behaviour has only been characterized along a few OTFs globally. Here, we use first-overtone Rayleigh waves extracted from seismic ambient noise to estimate the shear-wave velocity structure beneath the Blanco Transform Fault Zone (BTFZ). Compared to the adjoining normal oceanic plates, relatively variable and slow velocities reduced by at least $\sim 0.2\text{--}0.4 \text{ km s}^{-1}$ ($\sim 4\text{--}8$ per cent) are observed from the crust down to ~ 22 km depth along some segments of the BTFZ. The crustal slow velocities can be explained by enhanced fluid-filled porosity of $\sim 0.4\text{--}10.9$ per cent caused by intense fracturing associated with abundant seismicity. Slow uppermost mantle velocities are predominantly consistent with $\sim 1.2\text{--}37$ per cent serpentinization and ~ 9 per cent hydration, indicating variable and deep fluid infiltration that exceeds 15 km depth. For instance, shear-wave velocities ($\sim 4.3\text{--}4.4 \text{ km s}^{-1}$) in the uppermost mantle beneath the Blanco Ridge suggest extensive serpentinization ($\sim 13\text{--}25$ per cent), which might explain the recently documented earthquake swarms linked with aseismic creep. In comparison, within the vicinity of the ridge-transform intersections at depths $\sim >16$ km, low velocities ($\sim 4.1\text{--}4.2 \text{ km s}^{-1}$) that are consistent with the presence of up to ~ 1.6 per cent partial melt suggest intratransform magmatism which would contradict the long-held simple conservative strike-slip characterization of OTFs.

Key words: Crustal imaging; Seismic noise; Seismic tomography; Surface waves and free oscillations; Oceanic transform and fracture zone processes.

1 INTRODUCTION

Oceanic transform fault (OTF) systems are a plate boundary type that offset segments of mid-ocean spreading centres (Bird *et al.* 2002). OTFs, alongside their inactive fracture zones, are ubiquitous along the entire length of the mid-ocean ridge system, making them one of the most abundant linear features on the ocean floor. As first identified by Wilson (1965), they play a crucial role in the evolution of the lithosphere by creating room for the lateral motions of tectonic plates and providing connections between ridges and trenches (Hensen *et al.* 2019). OTFs can also host large earthquakes (e.g. the 2015 M_w 7.1 earthquake on the Charlie–Gibbs OTF along the Mid-Atlantic Ridge, the 2008 M_w 6.4 earthquake in the BTFZ and the 1994 M_w 7.0 Romanche earthquake; McGuire *et al.* 1996) and trigger tsunamis (Hensen *et al.* 2019). However, despite their geological importance, large portions of OTFs and fracture zones are still underexplored compared to their continental

counterparts. Consequently, their detailed origin, characteristics, evolution and dynamics which are pertinent to potentially better understanding the mechanisms of plate tectonics remain poorly understood.

According to plate tectonic theory, OTFs are conservative 2-D strike-slip plate boundaries where the lithosphere is neither created nor destroyed while it cools and deepens as a function of the age of the plate. This should result in fracture zones that are deeper than their parent transform faults. However, global bathymetric data show a contradicting pattern where seafloor beneath fracture zones is systematically shallower than their parent OTFs (Grevemeyer *et al.* 2021). With numerical simulation, Grevemeyer *et al.* (2021) explained this observation by proposing: (i) a two-stage crustal accretion process at both ridge-transform intersections (RTIs) and (ii) tectonic extension as the crust moves along the transform plate boundary. This implies that the crustal structure beneath OTFs may differ significantly from the crust found along fracture zones and

adjacent oceanic plates. Although sampling of fresh-looking basaltic rocks on the transform floor provide some evidence for volcanism along OTFs (e.g. Gaetani *et al.* 1995; Perfitt *et al.* 1996; Tepley *et al.* 2004), a complete picture of their potential magmatic evolution that includes how melt is extracted requires seismic imaging of the subsurface structure which have only recently become available along a few OTFs.

The availability of high quality seafloor bathymetric, magnetic and gravity data sets since at least the 1970s facilitated early morphological investigations of OTFs globally (e.g. Bonatti 1976, 1978; Bonte *et al.* 1982; Karson & Dick 1983; Abrams 1986; Gallo *et al.* 1986, 1987; Pockalny *et al.* 1988, 1997; Fornari 1989; Embley & Wilson 1992; Goff *et al.* 1993; Searle *et al.* 1994; Smith & Sandwell 1997; Dziak *et al.* 2000; Gregg *et al.* 2007; Gallo *et al.* 2012; Sandwell *et al.* 2014). Contrary to classical interpretations of a very simple OTF structure, some of these morphological studies have revealed important topographic anomalies, which indicate a more complex fault structure that reflect significant vertical tectonism (Bonatti 1976; Thompson & Melson 1972) and shearing along discrete transform fault segments (Fornari 1989). In many cases (e.g. Blanco, Siqueiros, Clipperton, Gofar and Quebrada in the Pacific, Doldrums, St Paul and Ascension in the mid-Atlantic and the Andrew Bain in the Southwest Indian ocean), the transform domains are segmented, comprising in a first-order sense a series of strike-slip faults offset by small intratransform spreading centres (ITSCs) or pull-apart grabens (Fornari 1989). The development of ITSCs, initiated by small changes in the pole of rotation of the bounding plates (Menard & Atwater 1968), is integral to the evolution of OTFs. Although ITSCs are distinguished by the morphologies and structural features of seafloor that flank their spreading centres which are mostly similar to those of mid-ocean ridges, observations of fresh lava flows and young basaltic rocks within the basin floor provide stronger constraints for their characterization. The absence of such extrusives at some proposed ITSCs (e.g. the Cascadia depression along Blanco) weakens the case for an active spreading ridge, thereby, protracting the debate about their true nature.

OTFs are also known to be structurally weak zones that facilitate the transmission of seawater into deeper parts of the oceanic lithosphere (Caine *et al.* 1996) where their interactions with crustal and uppermost mantle rocks exert some control on the composition and rheology of the fault zone (Rüpke *et al.* 2004; Faulkner *et al.* 2010). This has important implications on the ability of OTFs to host earthquakes and can be better understood by illuminating the relationship between the fault zone architecture and observed distribution of slip modes. Although some microstructural analysis of high strain peridotite mylonites recovered from Vema (Cipriani *et al.* 2009) and Prince Edwards OTFs (Kohli & Warren 2020), and deep seismicity in Romanche (Yu *et al.* 2021) and Blanco (Kuna 2020) indicate seawater may percolate to great depths, the true depth extent and variability of hydrothermal circulation beneath OTFs globally is still not well-quantified.

The structural complexities of OTFs that document their hydrothermal, tectonic and magmatic evolutions can be apparent in local to regional scale investigations using seismic tomography. Much of what we currently know about the nature of the crust and uppermantle structure beneath them come from previous active-source seismic refraction and reflection surveys in both fast- and slow-slipping transform environments (e.g. Bonatti 1976; Ibach 1981; Detrick *et al.* 1982; White *et al.* 1984; Calvert & Potts 1985; Ambos & Hussong 1986; Calvert *et al.* 1990; Vera *et al.* 1990; Detrick *et al.* 1993; Van Avendonk *et al.* 1998; Muller *et al.* 2000; Van Avendonk

et al. 2001; Marjanović *et al.* 2011; Roland *et al.* 2012; Maia *et al.* 2016; Gregory *et al.* 2021; Growe *et al.* 2021; Thomas *et al.* 2022; Wang *et al.* 2022). For instance, in the Atlantic and southwestern Indian Ocean dominated by slow-slipping transforms, the general consensus from these studies is that the subsurface structure is characterized by relatively thin, intensely fractured and hydrothermally modified crust, with a nearly absent gabbroic layer (e.g. Detrick *et al.* 1982, 1993; Muller *et al.* 2000). However, a recent study by Gregory *et al.* (2021) using wide-angle seismic data observed a thick (~6 km), likely mafic crust at the slow-slipping Romanche OTF. Along strike, OTFs can be highly heterogeneous, especially slow-slipping ones with large offset lengths (e.g. ~880 km for Romanche) so that isolated seismic reflection profiles may not be able to fully capture the complete underlying structure. The few studies that exist for fast-slipping OTFs of the Pacific Ocean (e.g. Bonatti 1976; Tréhu & Purdy 1984; Van Avendonk *et al.* 1998, 2001; Roland *et al.* 2012) reveal a relatively uniform thick crust [e.g. ~5.7 km in Clipperton; Van Avendonk *et al.* (2001), ~5.4 km in Orozco; Tréhu & Purdy (1984)] and low seismic velocities that extend throughout the crust interpreted as regions of severe fracturing and hydrothermal alteration associated with strike-slip faulting along active transform fault segments. Although active seismological studies do well in resolving small-scale seismic velocity heterogeneities expected along OTFs, they provide limited information about the broader lateral variation of the velocity structure and lithospheric structure below the Moho.

Since its first application (Shapiro *et al.* 2005), ambient noise tomography has shown to be an effective tool for imaging the crust and upper-mantle with relatively high resolution (e.g. Yang *et al.* 2007; Luo *et al.* 2012; Goutorbe *et al.* 2015; Adimah & Padhy 2019). It has already been applied at the Blanco Transform Fault Zone (BTFZ) situated in the northeastern Pacific ocean but in regional (e.g. Portritt *et al.* 2011; Gao 2016; Janiszewski *et al.* 2019) and continental (e.g. Zhang *et al.* 2021) frameworks that precluded a detailed characterization of the crust and uppermost-mantle structure beneath the transform fault. Also, most of these studies used relatively long period (~>10 s) fundamental mode surface waves that are barely sensitive to the oceanic crust (sensitivity peaks at depths ~>12 km for a starting oceanic model that consists of 3 km water and 0.1 km sediment overlying the crust and mantle). In this study, we analyse ~1-yr of seismic ambient noise data recorded by 67 OBSs deployed within the vicinity of the BTFZ to obtain short period (~4.0–8.0 s) first-overtone Rayleigh wave phase velocity dispersion curves. With the dispersion curves, we perform ambient noise tomography and then invert for a 3-D shear-wave velocity model down to a depth of 22 km which includes the crust and uppermost mantle. The robustly resolved seismic velocity structures observed along and around the BTFZ provide new and interesting insights into its crustal and uppermost mantle structural characteristics, evolution and dynamics.

2 ORIGIN, TECTONIC EVOLUTION AND SETTING

The BTFZ is a ~350-km-long intermediate-slipping (~56 mm yr⁻¹; Wilson 1993) OTF located off the southern Oregon coast in the northeast Pacific ocean. It is bounded by ~NE–SW trending Juan de Fuca and Gorda ridges to the northwest and southeast, respectively (Fig. 1). Its detailed origin and evolution like those of other OTFs have remained relatively controversial. Using existing plate

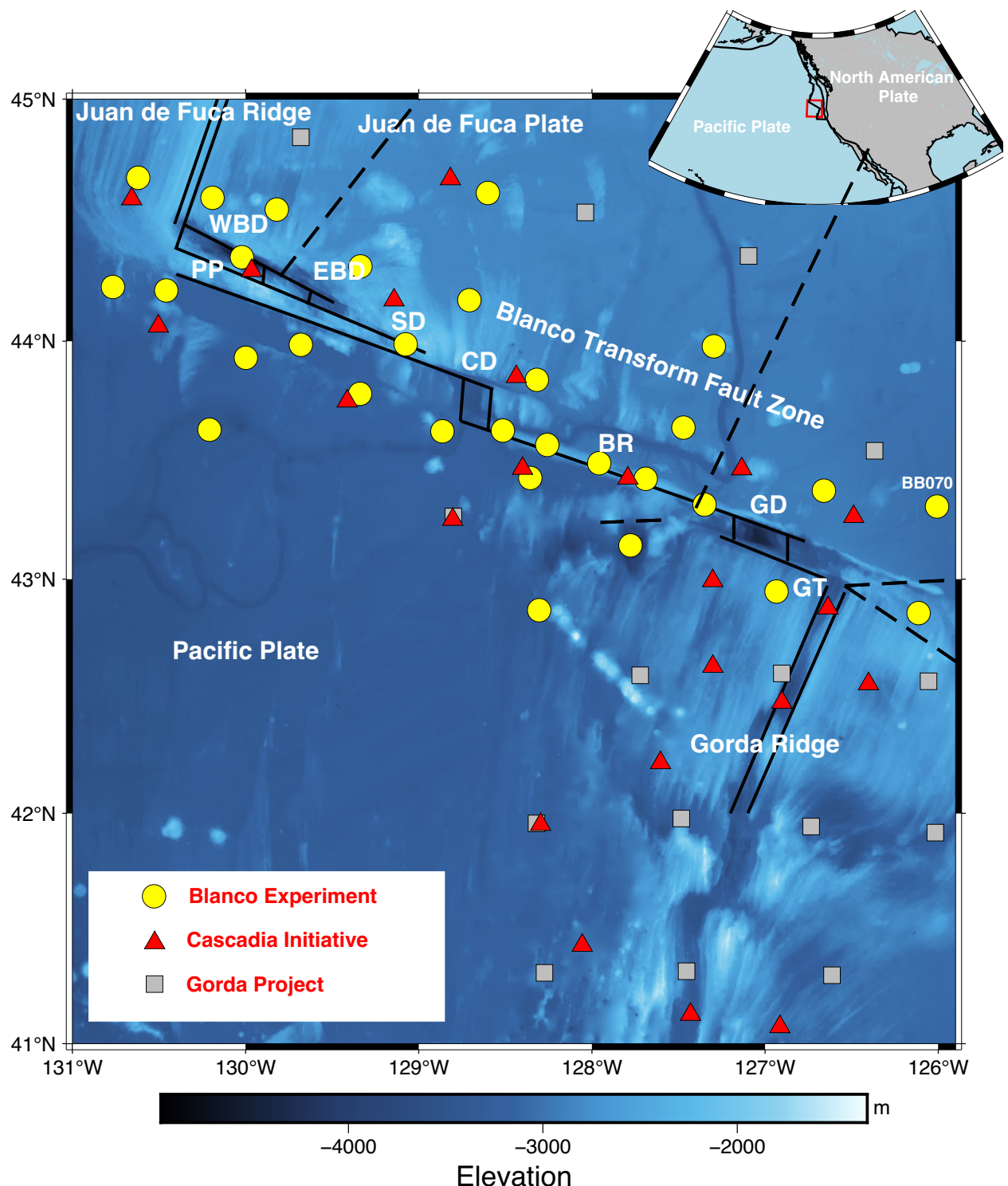


Figure 1. Topographic map of the study area showing the Blanco Transform Fault Zone (BTFZ) and broad-band stations of the Blanco experiment (Nabelek & Braunmiller 2012), the Cascadia initiative (Toomey *et al.* 2014) and the Gorda project (Nabelek & Braunmiller 2013). The red rectangle in the inset indicates the study region. The different segments of the BTFZ shown include WBD: Western Blanco Depression, EBD: Eastern Blanco Depression, SD: Surveyor Depression, CD: Cascadia Depression, PP: Parks Plateau, BR: Blanco Ridge and GT: Gorda Transform. The broken black lines outline approximate locations of pseudofaults (Wilson *et al.* 1984).

kinematic models developed from magnetic surveys (Hey & Wilson 1982; Wilson *et al.* 1984) as a framework, Embley & Wilson (1992) presented a model for the development of the BTFZ, supporting plate boundary reorganization by ridge propagation in response

to changes in the direction of relative plate motion. A clockwise shift of $\sim 15^\circ$ in the direction of the Juan de Fuca/Pacific relative plate motion occurring at ~ 5 Ma produced a major reorganization of the Juan de Fuca–Gorda spreading system that initiated the

formation of the BTFZ and established its location (Wilson *et al.* 1984; Wilson 1993). Subsequent series of ridge propagation events further reoriented and integrated the resulting transform fault and/or non-transform offset segments into the present day morphotectonic features of the BTFZ. Based on the lack of evidence for a stable transform fault segment before ~ 2 Ma within the BTFZ, in a recent modification to this model, Ren *et al.* (2023) argued that the early evolution of the BTFZ precluded discrete transform faults and instead involved the reorientation of non-transform offsets orchestrated by ridge propagation.

The BTFZ was first described by McManus (1967) as a series of ridges and troughs, striking at an azimuth of 118° . Recently acquired high resolution bathymetric data show the BTFZ to be highly segmented and morphologically marked by depressions and bathymetric highs (Embley & Wilson 1992). From the analysis of regional seismicity recorded by seismic stations deployed along the coast of Oregon, Braunmiller & Nábělek (2008) divided the BTFZ into a number of segments: eastern BTFZ which consists of the Gorda Depression (GD) and Blanco Ridge (BR); central BTFZ which comprises the Cascadia Depression (CD) and western BTFZ which consists of the Surveyor Depression (SD), Eastern Blanco Depression (EBD) and Western Blanco Depression (WBD, Fig. 1). With high resolution local seismicity data set, some recent studies (e.g. Kuna 2020; Ren *et al.* 2023) have further proposed additional segments such as the Gorda Transform (GT) and others in the western half that were poorly constrained by earlier regional scale studies. The BTFZ is highly seismically active and several studies (e.g. Braunmiller & Nábělek 2008; Kuna 2020; Ren *et al.* 2023) have reported a complex distribution of seismicity along its different segments. While the BR appears to be fully seismically coupled, plate motion in the western segments is mostly accommodated by aseismic creep (Braunmiller & Nábělek 2008).

The western BTFZ comprising of WBD, EBD and SD is the younger half of the BTFZ. It is structurally more complex and believed (on the basis of the difference between its average slip vector azimuth and the Pacific/Juan de Fuca relative plate motion) to be presently undergoing plate boundary reorganization. The WBD is a 60-km-long triangular \sim E-SE trending depression (Kuna 2020) located between the BTFZ-Juan de Fuca RTI and the EBD (Fig. 1). It is the deepest basin in the BTFZ (depth ~ 5 km; Ryan *et al.* 2009) intersected by three active sub-parallel transform fault strands with strikes between 290° and 296° (Kuna 2020). Between the WBD and SD is the 10×30 km 2 \sim NW-SE trending rhombohedral EBD, having a depth of ~ 3.7 km. Alongside three sub-parallel \sim NW-SE trending strike-slip fault strands, a series of 335 – 350° oriented ridges likely representing scarps of normal faults cut across the basin (Kuna 2020). The 5 km \times 20 km 2 rhombohedral SD bounded in the south by the narrow scarp Parks Plateau fault (Fig. 1) is the easternmost segment of western BTFZ (Kuna 2020). It is the smallest and shallowest basin (depth of ~ 3 km; Embley & Wilson 1992) in the BTFZ, dominated by normal faulting (see Fig. S1 in the Supporting Information for focal mechanism of a few main earthquakes along the BTFZ) with *T*-axes orientation oblique to the relative plate motion direction, indicating the pull-apart nature of deformation (Braunmiller & Nábělek 2008). The centrally placed CD roughly divides the BTFZ into two halves. Extending up to 50 km from its centre to the northwest and southeast, the CD is the largest depression in the BTFZ (Embley & Wilson 1992). It consists of a series of inward-facing back-tilted normal-faulting blocks oriented about 10 – 15° from orthogonal to the bounding transform faults (Dziak *et al.* 2000). Evidence of

igneous intrusions within the basin's sediment fill and orientation of the *T*-axes of the normal faults suggest the CD represents a short ITSC, interpreted to be the remnant of a southward growing ridge segment that dates back to ~ 5 Ma (Embley & Wilson 1992; Kuna *et al.* 2019).

The older eastern BTFZ comprises of the BR, the GD and the easternmost GT segments (Fig. 1). The ~ 150 -km-long BR sandwiched between the CD and GD is the most prominent bathymetric feature of the BTFZ. It consists of a transform fault that runs along the narrow (~ 4 – 7 km) ridge and trends at $\sim 111^\circ$, reaching heights of ~ 600 – 1700 m above the surrounding sea level (Braunmiller & Nábělek 2008; Kuna *et al.* 2019). Likely formed around ~ 1.6 Ma (Ren *et al.* 2023), several hypothesis have been proposed to explain the ridge uplift at BR that range from serpentine intrusions emanating from the lower crust and upper mantle (Bonatti 1976; Dziak *et al.* 2000) to dipslip component in the fault motion due to spreading direction changes (Thompson & Melson 1972) and compressional tectonism (Ibach 1981) have been proposed to explain the ridge uplift at BR. The geology of the BR is scantily known with only suites of greenstone and greenstone breccias collected from the eastern section (Hart *et al.* 1986) and a fragment of carbonate dredged from the western end near CD (Embley & Wilson 1992). The GD is a ~ 4.4 km deep rhombohedral basin that separates the BR and GT. It is the only identified basin in the eastern BTFZ (Fig. 1). Like the CD, the GD has been suggested to be a remnant spreading ridge that was almost replaced by the northward growing Gorda ridge about ~ 1 – 2 Ma (Embley & Wilson 1992; Ren *et al.* 2023). However, based on its rhombo-shaped geometry, it has also been interpreted to have probably formed by an extension between the northern and southern bounding strike-slip faults, making it appear like a mature pull-apart basin (Embley & Wilson 1992). The easternmost segment of the BTFZ is the GT. It was first identified from bathymetric data (Embley & Wilson 1992) and connects the BTFZ-Gorda ridge RTI and the GD.

3 DATA AND METHOD

3.1 Data

In the last few decades, several seismological experiments that deployed tens to hundreds of broadband seismic stations have been conducted in the NE Pacific. In this study, we collect approximately eight to twelve months of three component continuous seismic data recorded by 67 OBS stations from three different seismological experiments conducted in and around the BTFZ (Fig. 1 and Table S1 in Supporting Information). We also collect corresponding lengths of pressure records from colocated differential pressure gauge for each OBS. The Blanco experiment (Nabelek & Braunmiller 2012) provided 30 stations (Fig. 1) that operated approximately from September, 2012 to October, 2013. The Cascadia Initiative Community Experiment (Toomey *et al.* 2014) and the Gorda Project (Nabelek & Braunmiller 2013) provided 17 and 20 stations (Fig. 1), respectively. The Cascadia Initiative stations used in this study were in operation from September, 2012 to October, 2013 apart from two (J23C and J21C) that operated from September, 2013 to August, 2014 contemporaneously with the Gorda Project. Therefore, a total of 45 stations operated from September, 2012 to August, 2013 while the other 22 stations operated from September, 2013 to August, 2014. We retrieve all data from the Incorporated Research Institutions for Seismology Data Management Center (IRIS-DMC) where they are archived. Some sensors recorded data at 1 Hz while

others at higher rates of 50 and 100 Hz. We collect 1 Hz records where available and downsample those with higher sampling rates to 1 Hz.

3.2 OBS data corrections

The retrieval of reliable empirical Green's functions in ambient seismic noise tomography is contingent on the coherent wavefield that propagates between two seismic stations. OBS data contain more local noise compared to land-based stations, including those caused by tilting of seismometers due to ocean currents (tilt noise) and seafloor deformation caused by surface gravity waves (compliance noise, e.g. Webb & Crawford 1999; Crawford & Webb 2000). To improve the chances of extracting accurate and meaningful signals from OBS records, previous studies (e.g. Bell *et al.* 2014; Tian & Ritzwoller 2017; Adimah & Padhy 2019; Janiszewski *et al.* 2019; Yang *et al.* 2020; Russell & Gaherty 2021) have developed and/or applied different techniques to suppress these disruptive signals in the vertical component OBS data before using them for ambient noise tomography. Compliance and tilt noise corrections are achieved by removing coherent pressure and horizontal signals from the vertical channel, respectively. Although the pressure correction is typically applied at longer periods ($\sim > 25$ s) where linear surface gravity waves (infragravity waves) are dominant, its application at shorter periods ($\sim < 15$ s) within the microseism band has been shown to suppress fundamental mode energy, isolating the higher-mode Rayleigh wave information in the cross-spectra (Bowden *et al.* 2016; Yang *et al.* 2020; Russell 2021). As both the vertical and pressure channels in the $\sim 3\text{--}10$ s period band strongly record the fundamental mode Rayleigh interface waves sensitive to the water column, removing coherent pressure signals from the vertical channel in this band suppresses this water column arrival (Bowden *et al.* 2016). With the objective of extracting first-overtone Rayleigh waves in the $\sim 3\text{--}11$ s period band that are sensitive to our target oceanic crustal and uppermost mantle structures, we explore and take advantage of these observations. First, we remove the instrument responses from the raw data then remove coherent pressure and horizontal energy from the vertical component records broadly following the transfer function technique presented by Bell *et al.* (2014) which is somewhat similar to that of Crawford & Webb (2000). It entails calculating a transfer function of the vertical component, for non-vertical components, representing the tilt and compliance (< 25 s) or water-seafloor interface wave ($\sim 3\text{--}11$ s) noise. They are then systematically subtracted from the vertical component records to give the noise-corrected vertical component data. A more detailed step-by-step description of how we implement the correction can be found in Adimah & Padhy (2019). An example of raw- and noise-corrected vertical component records at OBS BB070 (Fig. 1) shown in Figs S2(b) and (c) in the Supporting Information demonstrates significant reduction in the noise levels after denoising. The power spectrum densities (PSD) of the raw and denoised records in Fig. S2(d) also show decrease in noise levels in the cleaned record across the entire time period.

3.3 Ambient noise cross-correlation analysis

To obtain high quality cross-correlation functions (CCFs) from the noise-corrected vertical component OBS data, we follow the well established noise processing routine described by Bensen *et al.* (2007). We deploy a high-performance python tool for ambient-noise seismology (Noisepy; Jiang & Denolle 2020) that provides

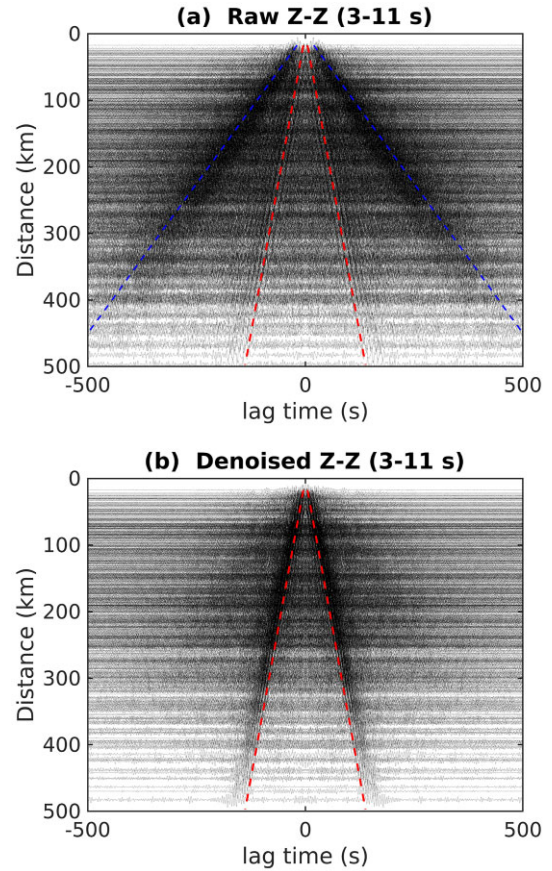


Figure 2. All bandpass filtered ambient noise CCFs. (a) Without suppression of tilt and compliance. Fundamental and higher mode Rayleigh wave energies are present. Group velocities of 3.6 and 0.9 km s^{-1} are indicated by the red and blue dashed lines, respectively. (b) Tilt and compliance noise suppressed before calculating the CCFs resulting in the dominance of the Rayleigh wave first-overtone energy.

most of the processing techniques for ambient noise data. These processing steps are briefly recounted here. First, we perform basic preprocessing on individual station $\sim 8\text{--}12$ months continuous data such as downampling into 1 Hz for higher sampled data, cutting into small window lengths of 8 hr, demeaning, detrending and tapering using a Tukey window with 5 per cent cosine taper on both ends. This is followed by $2.5\text{--}25$ s ($0.04\text{--}0.4$ Hz) bandpass filtering before the application of temporal normalization (running-absolute-mean method used) and spectral whitening. The time-domain normalization suppresses the effects of earthquakes and other transient signals which act to obscure the noise signal, while spectral whitening helps to broaden the band of the ambient noise signal in the CCF (Bensen *et al.* 2007). Next, we perform 8-hourly cross-correlations followed by stacking over the entire $\sim 8\text{--}12$ months period to obtain the final stacked CCF cross-spectrum for each seismic station pair. Cross-correlation is performed separately for the two different station operating windows of 2012–2013 (45 stations) and 2013–2014 (22 stations), giving a total of 1221 CCF cross-spectra.

To highlight the effects of tilt and compliance noise correction on the CCFs, we also process and analyse the raw OBS data in a similar fashion. Due to the non-uniform azimuthal distribution of noise sources, the CCFs are asymmetric (Roux *et al.* 2005). We average the positive and negative time lags of each CCF to minimize this effect. In Fig. 2, we plot the raw and denoised stacked

CCFs for all station pairs bandpass filtered in the 3–11 s period band. The denoised stacked CCFs (Fig. 2a) are dominated by the first-overtone Rayleigh waves with the fundamental mode information almost completely absent. For the raw cross-spectra (Fig. 2b), the fundamental and first higher modes are present with comparable strengths. Clearly, the application of the pressure correction contributes to the isolation of the first-overtone information in the short period band as also observed by Bowden *et al.* (2016) and Yang *et al.* (2020) in regions offshore California and in the central Pacific, respectively. Mode isolation is an important step in surface wave analysis as earth structure retrieved using data in which the different modes are not properly separated could be biased.

3.4 Phase velocity dispersion measurement

Only noise-corrected cross-spectra in which the first-overtone Rayleigh waves are conspicuous and dominant are used for further analysis. We adopt the cross-spectra waveform fitting technique of Menke & Jin (2015) to measure the interstation phase velocities from 3 to 11 s periods. The technique involves fitting a Bessel function to the observed cross-spectra based on the cross-spectra formulation of Aki (1957):

$$\rho(\omega, r) = A J_0 \left(\frac{\omega r}{c(\omega)} \right) \quad \text{with } A = 1, \quad (1)$$

where ρ is the real part of the cross-spectra, $c(\omega)$ is the interstation phase velocity at frequency ω , r is the interstation distance, J_0 is the Bessel function of order zero and A is the amplitude factor added to model attenuation and errors in normalization of the cross spectrum (Menke & Jin 2015). This method performs well for low SNR and short interstation distance cross-spectra that generally characterize OBS deployments as used in this study. The Bessel fitting has been observed to be sensitive to the starting dispersion model (e.g. Janiszewski *et al.* 2019) so that the use of an arbitrary *a priori* starting dispersion curve may bias the result. To avoid this pitfall, we first obtain the average phase velocity dispersion curve of the first-overtone Rayleigh wave to be used as the starting model. The high-resolution linear Radon transform (LRT) technique (Luo *et al.* 2008, 2015) whose detailed procedure is well documented in Luo *et al.* (2008, 2009, 2018) is applied. The technique leverages seismic array observations to extract dispersion information from multimode surface waves that may interfere in the time domain. Through the solution of an inverse problem, the LRT transforms the seismograms in the time–distance domain to the period–phase velocity domain where the different modes have distinguishable branches. With the suit of 1221 CCFs bandpass filtered in 3–10 s, here, we use the conjugate gradient algorithm to solve the inverse problem, setting the model and residual weighting as described by Ji (2006). The resulting LRT panel is shown in Fig. 3. Although we see traces of the fundamental mode at periods ~ 9 s and the second higher mode at periods ~ 4 s, the first-overtone energy dominates as expected.

We perform the Bessel fitting twice for each cross-spectrum, using a nonlinear least squares algorithm. For the first, the average phase velocity dispersion measurement (red line in Fig. 3) is used as the starting model. In the second, the result from the first inversion is used as starting dispersion model. This approach appears to reduce the degree of cycle skipping in the final Bessel fits and has a more physical basis compared to the grid search approach of determining a starting model. Examples of this procedure showing the cross-spectra, Bessel fits and obtained dispersion curves for a variety of interstation distances and SNR are shown in Figs 4 and

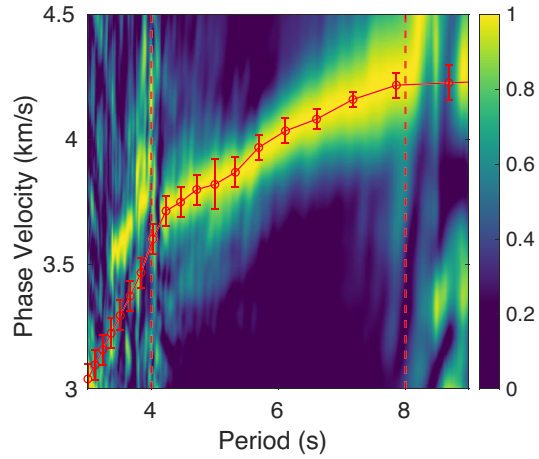


Figure 3. Array-averaged Rayleigh wave phase velocity dispersion measurement obtained using the high-resolution linear radon transform. The first-overtone Rayleigh wave dispersion curve as shown by the solid red line is robustly measured between ~ 4 and ~ 8 s periods indicated by the dashed vertical red lines. It is used as the starting model to estimate interstation phase velocity dispersion measurements. The color bar represents the normalized energy contained in the different surface wave mode branches.

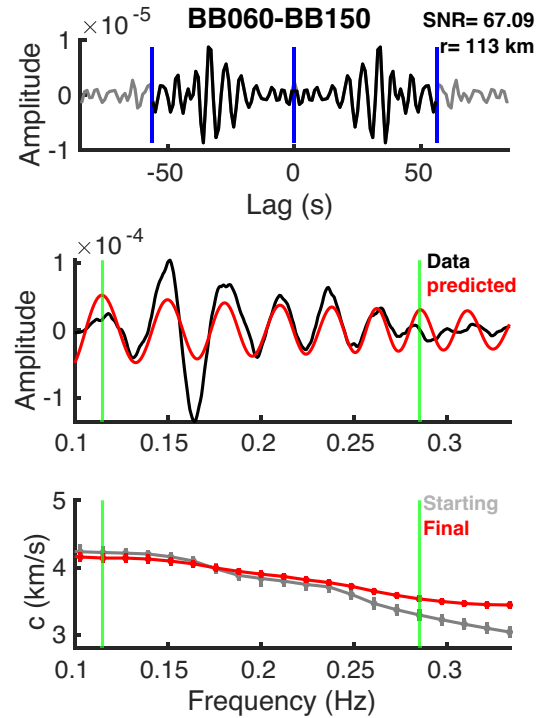


Figure 4. An example of interstation phase velocity estimation using the cross-spectra waveform fitting technique. Top panel: interstation cross-correlation function with the vertical blue lines marking the 2.0 km s^{-1} group velocity. Middle panels: Bessel function fitting where the red and black curves indicate the Bessel function and real part of the CCF, respectively. Bottom panels: Dispersion measurement with the red and grey lines indicating the extracted and starting phase velocities, respectively. The vertical green lines indicate the period band of 3.5 and 8.7 s where measurements are reliable.

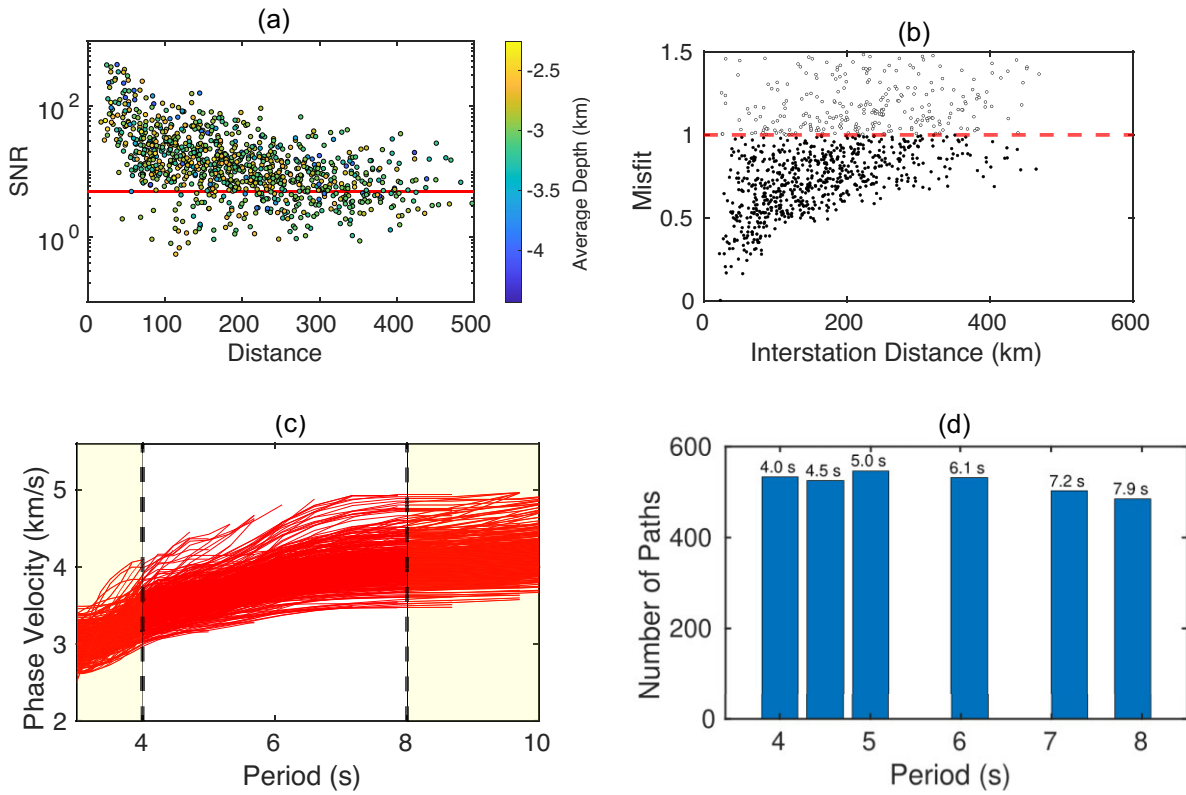


Figure 5. (a) SNR distribution of the CCFs with interstation distance and average station pair depth. SNR = $\text{RMS}(\text{signal})^2 / \text{RMS}(\text{noise})^2$, where signal is defined as any arrival with group velocity $>1.5 \text{ km s}^{-1}$. The horizontal red line indicates the SNR cutoff of 5 passed by 952 measurements. (b) Misfit between the observed and predicted cross-spectra. To ensure only the highest quality measurements are used for tomographic inversion, we use misfit cutoff of 1.0 shown by the horizontal red dashed line after testing different cutoffs ranging from ~ 0.7 to 1.5. (c) The suite of all dispersion curves. (d) Number of interstation dispersion measurements used for tomography at six continuous time periods.

S3. As a result of decrease in signal strength at the extreme periods ($\sim >9$ and $\sim <3.5$) as reflected by the relatively poor Bessel fits (middle panels of Figs 4 and S3), we decide to only consider dispersion measurements in the period range 3.5–8.7 s as windowed by the vertical green lines in the middle and bottom panels of Fig. 4.

To ensure that only high quality and reliable phase velocity dispersion measurements are selected and used for tomographic inversion, we impose several quality control measures (e.g. Figs 5a and b). The time-domain surface wave dispersion measurement methods require interstation distance of at least three wavelengths (Bensen *et al.* 2007) to extract a reliable dispersion measurement at a given period. However, frequency-domain methods like the cross-spectra waveform fitting technique we have used give reliable measurements even at one wavelength. Here, we conservatively apply interstation distance of at least two wavelengths. Secondly, we set signal-to-noise ratio (SNR) ≥ 5 , so that dispersion measurements obtained from CCFs with SNR less than 5 are rejected (Fig. 5a). Here, SNR is defined as the ratio of the root-mean-square of the signal window to the root-mean-square of the noise window, where the signal window is defined by arrival times corresponding to group velocities greater than 1.5 km s^{-1} , and the remaining window represent the noise window. Third, we reject measurements where the misfit between the Bessel and real cross-spectrum curve is > 1.0 (Fig. 5b). Finally, we visually inspect the results to discard obviously bad measurements that may have passed the quality control measures. The suite of 660 phase velocity dispersion curves that passed the quality control

measures and available for surface wave tomography is shown in Fig. 5(c). It shows velocity variation of up to 20 per cent which indicates substantial structural heterogeneity in the region. A similar significant amount of velocity variation is also observed for the suite of dispersion curves strictly sampling the BTFZ (Fig. S4a), suggesting a relatively complex crust and uppermost mantle structure beneath the transform plate boundary that reflect its various morphotectonic features.

3.5 Phase velocity tomography

The ultimate goal of this research work is the estimation of a 3-D isotropic shear-wave velocity model of the crust and uppermost mantle, spanning the entire BTFZ and adjacent oceanic lithospheres. To achieve this, we follow a two-step approach that includes (1) inversion for first-overtone Rayleigh wave phase velocity maps at discrete periods between 4.0 and 8.0 s (shorter and longer period measurements conservatively discarded) and (2) extraction and inversion of local nodal first-overtone Rayleigh wave dispersion curves for isotropic 1-D shear-wave velocity structures that will be thereafter compiled to give the final 3-D shear-wave velocity model of the study region.

In this section, we describe the first step in which we use reliable dispersion curves to invert for 2-D first-overtone Rayleigh wave phase velocity maps at 11 distinct periods between 4.0 and 8.0 s. We implement the widely used ray theory that assumes the seismic

surface waves as rays that propagate along great circle paths connecting sources and receivers (in this case station pairs). Expressed in terms of phase-slowness, the forward problem is conveniently linear with each frequency-dependent travel time measurement obtained by integrating the phase-slowness along the wave path. We adopt a linearized iterative least-squares inversion scheme (Menke 2012) with regularization delivered by data-uncertainty-weighted second derivative smoothing. Based on a series of checkerboard resolution tests discussed in the subsequent subsection, we parameterize the study area into a uniform grid system of $0.1^\circ \times 0.1^\circ$ and apply optimal regularization strengths across all investigated period. To further identify and weed out bad measurements, the inversion is performed twice in a systematic manner. In the first run, the inversion is performed for all selected dispersion data with associated estimated measurement uncertainties as obtained from the cross-spectra waveform fitting. Data residual for each datum including its mean and standard deviation at each period are calculated. In the second step, data with absolute residual ≥ 2 times the standard deviation of all residuals at each investigated period are discarded before performing the inversion. Fig. 5d shows the final number of phase velocity dispersion measurements used for the tomographic inversion at six selected periods between 4.0 and 8.0 s. Examples of distributions of phase travel time misfits calculated as the difference between the observed phase times and predictions from the final estimated Rayleigh wave velocity maps at selected periods are shown in Fig. S5. Apart from the 5.0 s period (Fig. S5c), the standard deviation increase with period to a maximum of about 1.32 s at the 7.2 and 7.9 s periods (Figs S5e and f). This trend can be attributed to decreasing SNR with increase in period, indicating relatively poorer data quality at the longer periods. However, the mean misfit is generally < 1 s across all investigated periods, capturing how well outliers were removed from the data.

The straight-ray method we have used in this study does not correct for finite-frequency effects like scattering, multipathing, diffraction, etc. unlike other sophisticated methods (e.g. eikonal and Helmholtz tomography) that also deliver robust uncertainties alongside the resulting group or phase velocity maps. However, some studies that have compared tomographic maps from straight-ray and eikonal methods (e.g. Lin *et al.* 2009; Shen *et al.* 2016; Feng & Ritzwoller 2019) found similar velocity variations in both, with the straight-ray tomographic maps, as expected, only slightly faster than eikonal ones. In a study to investigate the influence of different assumptions about the propagation of surface waves in seismic tomography, Godfrey *et al.* (2019) favoured great-circle ray approximation based on similar tomographic results obtained using ray and finite-frequency theories. Notwithstanding, we made efforts to further examine the robustness of our straight-ray tomographic maps by applying the finite-frequency kernels method of Lin *et al.* (2009) to our dispersion data. Although the analytical sensitivity kernels we used (eq. 11 in Lin *et al.* (2009)) do not account for ray bending away from the great circle, it takes care of finite-frequency effects. In any case, short interstation distances that dominate our dispersion measurements suggest negligible amount of ray bending. The results displayed in Fig. S6 of the Supporting Information, overall, show similar features as those of our straight-ray tomography (Figs 6 and S7) but slower across all investigated periods. Therefore, we conclude that straight-ray tomography is reliably applicable and suffices in instances like this where data quantity and quality inhibits the use of more sophisticated techniques like the eikonal method, which requires reconstructing

the phase-delay surface for each virtual source. The slight difference in absolute velocity between both methods will be taken into consideration when interpreting our straight-ray tomographic maps (Fig. 6).

3.6 Synthetic recovery tests and sensitivity kernel analysis

Prior to phase velocity tomographic inversion, we performed a series of checkerboard resolution tests to determine the ability of our data to resolve structural anomalies of different sizes and the optimum inversion parameters. We construct synthetic models having anomaly sizes of 0.25° , 0.4° , 0.5° , 0.6° , 0.7° , 0.9° and 1.0° with alternating velocities of ± 10 per cent from the mean velocity of 3.5 km s^{-1} . For each synthetic model and at each period, using identical paths available for the real data, we compute the travel times for each path. With the same tomographic inversion scheme used for the real data, the synthetic travel times are inverted using different model parameterizations and inversion parameters. Analysing the multitude of results, in general, the checkerboard patterns are well retrieved using model parametrization of $0.1^\circ \times 0.1^\circ$ and smoothing weights lying between 1 and 5. Fig. S8 shows the recovered checkerboard patterns for the different anomaly sizes at 4.0, 5.0 and 7.9 s periods. Along the BTFZ and the immediate adjacent Juan de Fuca and Pacific oceanic plates, checkerboard sizes of $0.5^\circ \times 0.5^\circ$ to $1.0^\circ \times 1.0^\circ$ are relatively well recovered, although with reduced amplitude, especially for the $\leq 0.5^\circ \times 0.5^\circ$ pattern (Figs S8a–i). While not the focus of the current study, northern and central sections of the Gorda ridge are similarly fairly retrieved. Towards the peripherals of the study area, especially the northern and southern edges, the recovery degrades and smearing is observed. For the smallest anomaly size of $0.25^\circ \times 0.25^\circ$ shown in Figs S8(a)–(c), the recovery is relatively poor. On the basis of these tests, we focus on interpreting seismic velocity anomalies along the BTFZ and its immediate adjacent regions where our data show optimal resolution of ~ 55 km.

At virtually all investigated periods of our phase velocity tomographic maps (Fig. 6), several regions along the BTFZ are delineated by slower velocities compared to the immediate adjacent oceanic lithospheres. To ascertain the robustness and reliability of this feature, we perform a synthetic recovery test for the geometry of the BTFZ. A test model in which the BTFZ is represented by a ~ 350 km long slow velocity structure (-5 , -8 and -10 per cent perturbation from the background velocity of 3.0 km s^{-1}) with a variable width that has a maximum value of ~ 30 km (Figs S9.1a, S9.2a and S9.3a) is constructed. Based on the test model, synthetic data is computed and inverted using the same model parameterization and inversion parameters used for the real data. As shown in Figs S9.1(b)–(g), S9.2(b)–(g) and S9.3(b)–(g), the input slow velocity structures are fairly well retrieved across the selected periods with some lateral smearing. Overall, results from both synthetic tests are encouraging, confirming that our data and parameterization are sufficient to recover seismic velocity anomalies of ~ 40 – 50 km but with diminished amplitudes across all periods of interest beneath the study region.

To estimate the depth ranges of sensitivity of our first-overtone Rayleigh-wave phase velocity maps at the different periods which will serve as a guide for their interpretations, we calculate their sensitivity kernels using surf96 (Herrmann & Ammon 2004). Firstly, we perform a linearized iterative inversion (Herrmann & Ammon 2004) of the array-averaged phase velocity dispersion curve (Fig. 3)

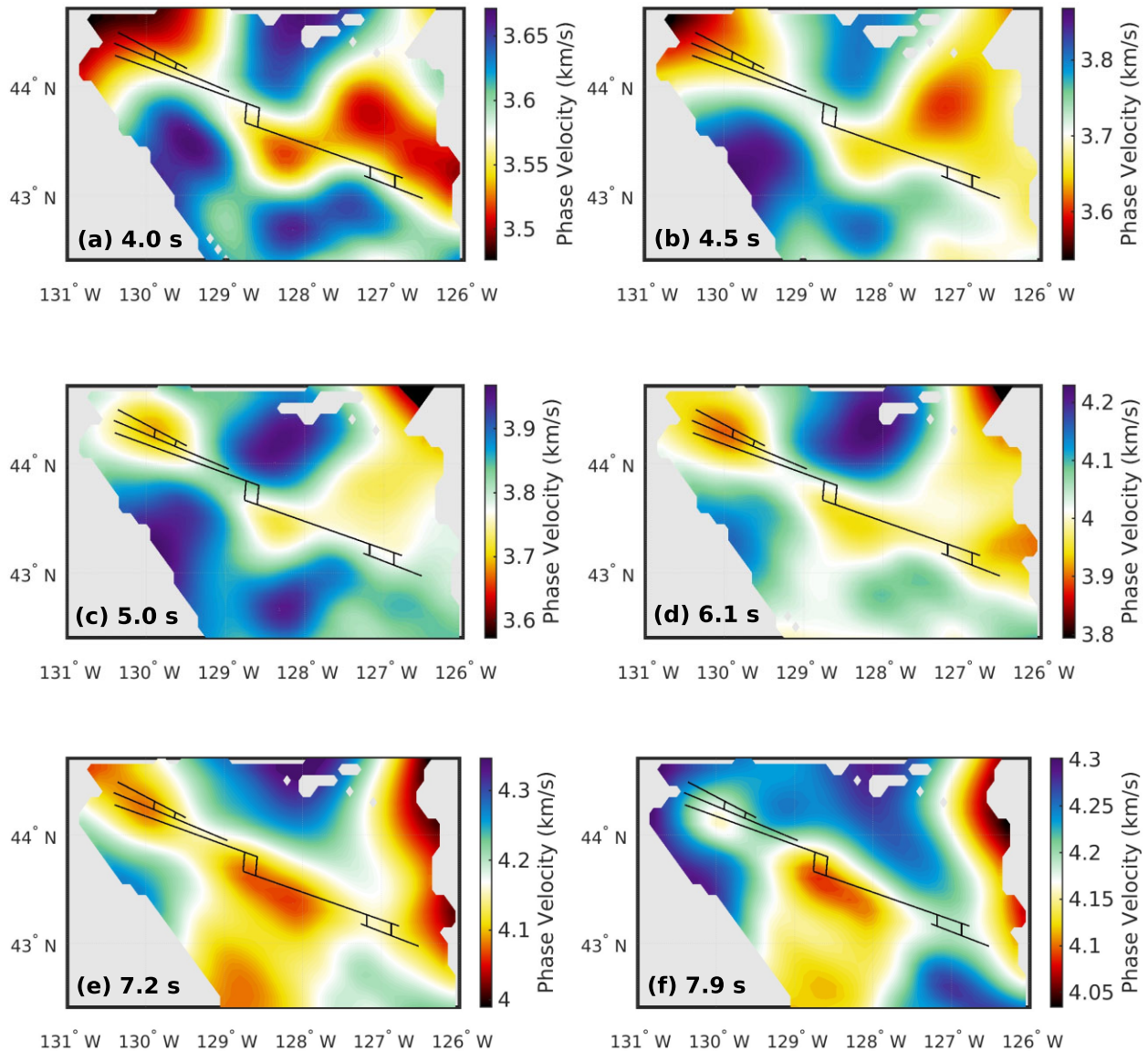


Figure 6. First-overtone Rayleigh wave phase velocity tomographic maps at six discrete time periods of 4.0, 4.5, 5.0, 6.1, 7.2 and 7.9 s. The black lines indicate the approximate location of the Blanco Transform Fault. Peripheral regions with poor raypath coverage are masked out.

to obtain the array-averaged 1-D shear-wave velocity profile (red line in Fig. 7a). The starting 1-D shear-wave velocity model (blue line in Fig. 7a) including P -wave velocity and density for the inversion are obtained from previous tomographic studies over the NE Pacific (e.g. Gao & Shen 2015; Bell *et al.* 2014, 2016; Gao 2018). It is parametrized with a 3.5 km water layer, 0.5 km sedimentary basin and a 5-km-thick crust overlying the upper mantle. In general, the sensitivity kernels (Fig. 7b) show that our investigated periods of 4.0–8.0 s are sensitive to shear-wave velocity structure from the seafloor to a depth of ~ 25 –30 km. Peak sensitivities of the 4.0, 5.0, 6.0, 7.0 and 8.0 s periods are at approximate depths of 5, 9, 12, 15 and 17 km, respectively. In particular, the shortest period of 4.0 s is strongly sensitive to the near surface structures while the 5 s period map is sensitive to crustal shear-wave velocity. The longer periods of 6.1, 7.2 and 7.9 s are sensitive to the deeper structures in the uppermost mantle.

3.7 Inversion for shear-wave velocity

Before inverting for the shear-wave velocity model, the phase velocity tomographic maps are further smoothed into a coarser grid of $0.3^\circ \times 0.3^\circ$ which results in a total of 238 gridpoints for the study area. At each gridpoint of the smoothed phase velocity maps, a local first-overtone Rayleigh wave phase velocity dispersion curve is extracted for eleven distinct periods between 4.0 and 8.0 s, then inverted for 1-D shear-wave velocity structure using a linearized iterative least-squares inversion scheme (*surf96* – Herrmann & Ammon 2004). We tested several model parameterizations that include B-splines and stack of horizontal layers with varying thicknesses before adopting a 3-D layered model that consists of water and sediment layers, a 6-km \times 1-km-thick crust, a 10-km \times 2-km, 4-km \times 5-km and 4-km \times 10-km-thick upper mantle, overlying a half-space. Crustal and upper mantle shear-wave velocities in the

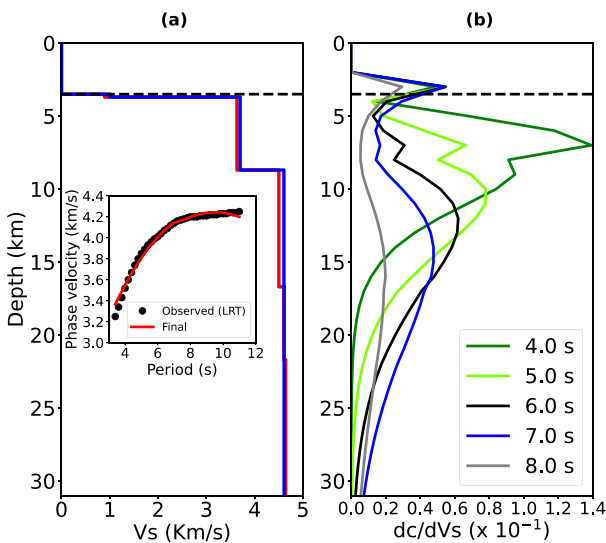


Figure 7. (a) Linearized iterative inversion of the array-averaged dispersion curve. The inset shows the fit between the observed (black solid circles) and predicted (red curve) phase velocity dispersion curves. The blue and red lines are the starting and final 1-D shear-wave velocity structures, respectively. (b) first-overtone Rayleigh wave phase velocity sensitivity kernels with respect to the array-averaged shear-wave velocity structure (red line in panel a) for time periods between 4.0 and 8.0 s investigated in this study. The horizontal black dashed lines indicate the 3.5 km water depth.

reference starting model are obtained from the average 1-D shear-wave velocity profile of the study area (Fig. 7a). Corresponding *P*-wave velocities are scaled from the shear-wave velocities while density structure is obtained from *P*-wave velocities using empirical relations of Brocher (2005). Bathymetry in the vicinity of the BTFZ is complex and varies relatively strongly (contrast reaching up to ~ 1600 m) as seen in Fig. 1. The excitation and propagation of surface waves, especially high frequency/short wavelength Rayleigh waves, have been shown to be substantially affected by topography/bathymetry and sediment thickness (Gualtieri *et al.* 2015; Wehner *et al.* 2022), so that ignoring them in tomographic inversions could introduce some bias into the results. Although the wavelength of the shortest period (4 s) Rayleigh waves in our analysis is much greater than the largest bathymetric contrast in the study area (assuming Rayleigh-wave phase speed of 3 km s^{-1}), we perform the inversion with true bathymetry. We use bathymetry data from Tozer *et al.* (2019) as shown in Fig. 1 and sediment thicknesses from NOAA's global map (Divins 2003). To stabilize the shear-wave velocity inversions, we apply a 16-point linear interpolation to the eleven phase velocity measurements and mildly smoothen water depths at a few gridpoints where there is relatively strong variation in bathymetry of more than 1 km.

Knowing that the inversion of surface wave dispersion data for shear-wave velocity using linearized iterative inversion techniques can be sensitive to the initial velocity model, we generated a suite of 50 starting models for each gridpoint by perturbing the reference starting model, following a uniform distribution within 25 and 15 per cent in the crust and mantle, respectively. The water depths and sediment thicknesses are kept constant. At each gridpoint, all 50 starting models are then inverted for shear-wave velocity only. After 40 iterations, we observe relatively good fit between the synthetic and measured dispersion curves, signifying model convergence. During each inversion, minimal smoothing and damping

are enforced systematically to avoid unrealistic variations in velocity across layers. The fifty constrained models form an ensemble of 1-D shear-wave velocity profiles whose mean and standard deviation are computed, representing the final shear-wave velocity structure at each gridpoint. Two examples of the inversion procedure are shown in Fig. 8. Finally, all 238 mean shear-wave velocity structures are compiled into a 3-D shear-wave velocity model of the study region.

4 RESULTS

In this section, we present and describe the main results of the study that include the first-overtone Rayleigh-wave phase velocity maps (Fig. 6) and the 3-D isotropic shear-wave velocity model (Figs 8, 9, 10 and 11), down to a depth of ~ 22 km.

4.1 Phase velocity maps

Our first-overtone Rayleigh-wave phase velocity tomographic maps at periods of 4.0, 4.5, 5.0, 6.1, 7.2 and 7.9 s are shown in Fig. 6. A summary of tomographic maps at all eleven periods between 4.0 and 8.0 s investigated in this study are shown in Fig. S7. In general, several regions along the $\sim 10\text{--}40$ km wide BTFZ are characterized by slow phase velocities relative to the immediate adjacent Juan de Fuca and Pacific plates, across all investigated periods from 4.0 to 7.9 s (Figs 6 and S7). The resolution of our data (~ 55 km) is insufficient to completely resolve the smaller segments like the SD where the observed slow velocities are less apparent. Nonetheless, this is an important feature of our tomographic model which is consistent with several lines of evidence that indicate transform fault zones to be significantly damaged in contrast to their surrounding normal oceanic lithosphere (Cox *et al.* 2021). The average phase velocities range from $\sim 3.55 \pm 0.1 \text{ km s}^{-1}$ at 4.0 s period to $\sim 4.2 \pm 0.2$ at 7.9 s period (Figs 6 a and f). At the shortest periods of 4.0–5.0 s (Figs 6a–c and Figs S7a–e), phase velocity is mostly sensitive to sediments, the upper and lower crust (Fig. 7). The slowest velocities ($\sim 3.5\text{--}3.7 \text{ km s}^{-1}$) along the strike of the BTFZ at these periods roughly coincide with the locations of the western and central BR, WBD and the BTFZ-Juan de Fuca ridge RTI. Moving towards eastern BTFZ from the WBD, the slow velocity zone becomes slightly faster and narrower, especially around the SD and regions preceding the CD. Approximately within the CD and western BR, the slow velocity zone broadens and slightly intensifies. The slowest velocities off the strike of the BTFZ are observed in the southeastern section of the Juan de Fuca Plate bordering eastern BR, GD and GR to the north. These slow velocity structures are quite intense at periods $\sim < 5$ s and become less apparent at longer periods. Overall, at these short periods, phase velocities within the Pacific Plate (south of the BTFZ) are generally faster than those on the Juan de Fuca Plate.

The longer periods ($\sim > 5$ s), especially 6.1, 7.2 and 7.9 s (Figs 6d–f and Figs S7f–k) are sensitive to the uppermost mantle structure, down to a depth of ~ 22 km (Fig. 7). Similar phase velocity patterns as seen at the 5 s period map with slight variations are observed in the 6.1 s period map. Here, the distinct slow phase velocities along central BTFZ and western BR appear to elongate along strike into eastern BR and the GD. They also spread out into the adjacent central Pacific Plate, southward. Just like at 4–5 s period, fast phase velocities ($\sim 4\text{--}4.2 \text{ km s}^{-1}$) dominate both adjacent oceanic plates with slightly varying intensities, typical for normal oceanic lithospheric mantle. At the longest periods of 7.2 and 7.9 s, the phase velocity variation patterns are identical. The slowest velocity anomaly mostly along western BR at the 7.2 s period appears to

be narrowed, further elongated (compared to the preceding period of 6.6 s in Fig. S7) and more aligned with the ridge. South of this anomaly in the Pacific Plate, an isolated slow velocity zone persists into the 7.9 s period map with reduced intensity, spreading out towards the BR. At these periods, much of the Pacific Plate is dominated by slower velocities compared to the Juan de Fuca Plate. Although beyond the scope of this study, across some of the investigated periods (e.g. 4.0, 4.2, 5.7 and 6.1 s), the northern and central sections of the Gorda ridge are broadly delineated by

slightly slower velocities compared to the bounding adjacent Pacific and Gorda plates (Fig. S7). At ≥ 10 s periods, Zhang *et al.* (2021) also observed a similar pattern in their phase velocity maps.

4.2 Shear-wave velocity model

Fig. 8 shows examples of 1-D shear-wave velocity structures and uncertainties (represented by one standard deviation of the ensemble of final shear-wave velocity profiles at each grid node) at

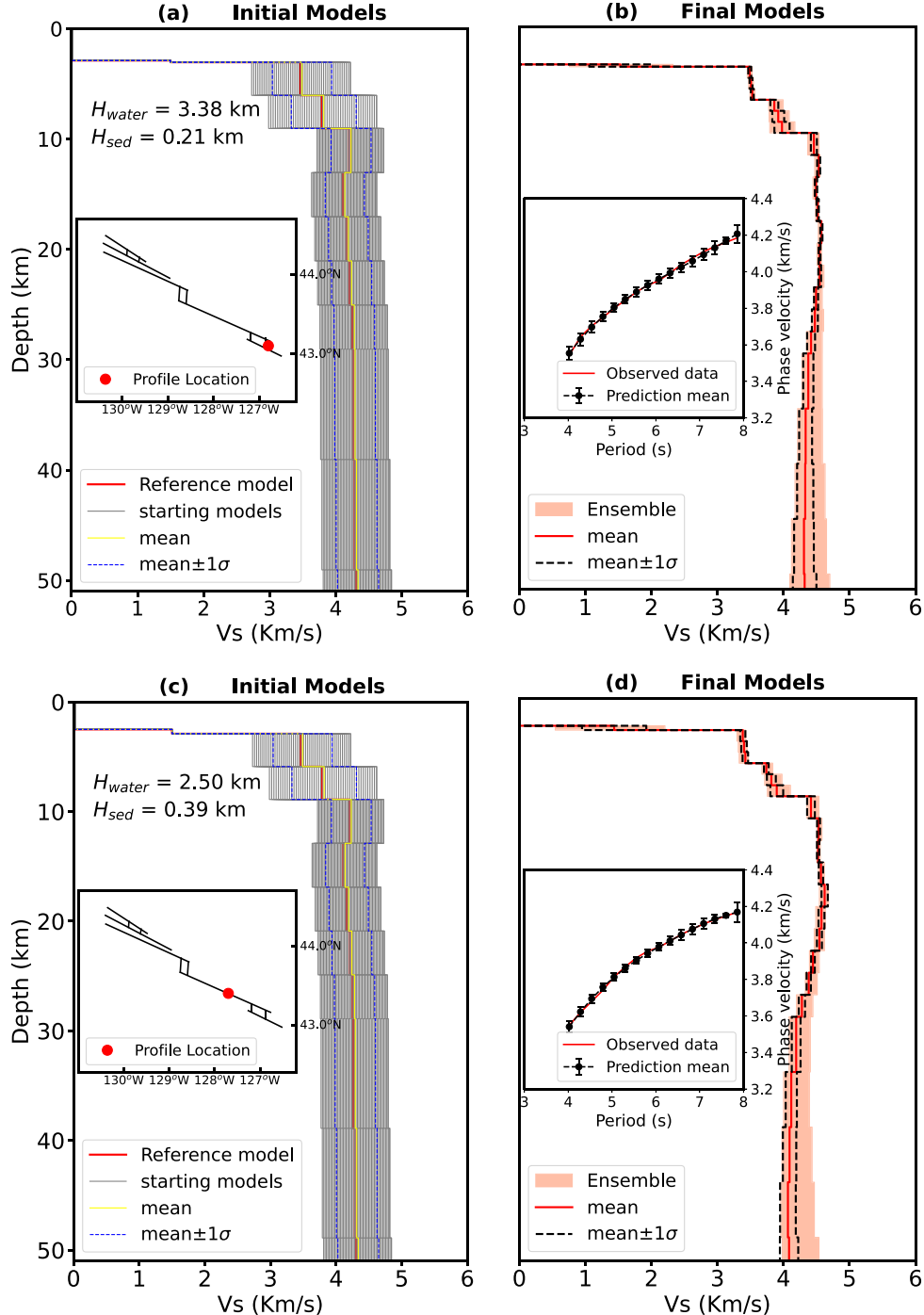


Figure 8. Examples of 1-D V_s inversion at a node approximately within Gorda Depression (a, b) and along the Blanco Ridge (c, d). H_{water} and H_{sed} are water depth and sediment thickness, respectively. The short vertical bars in the predicted mean dispersion curves indicate the range of the predictions.

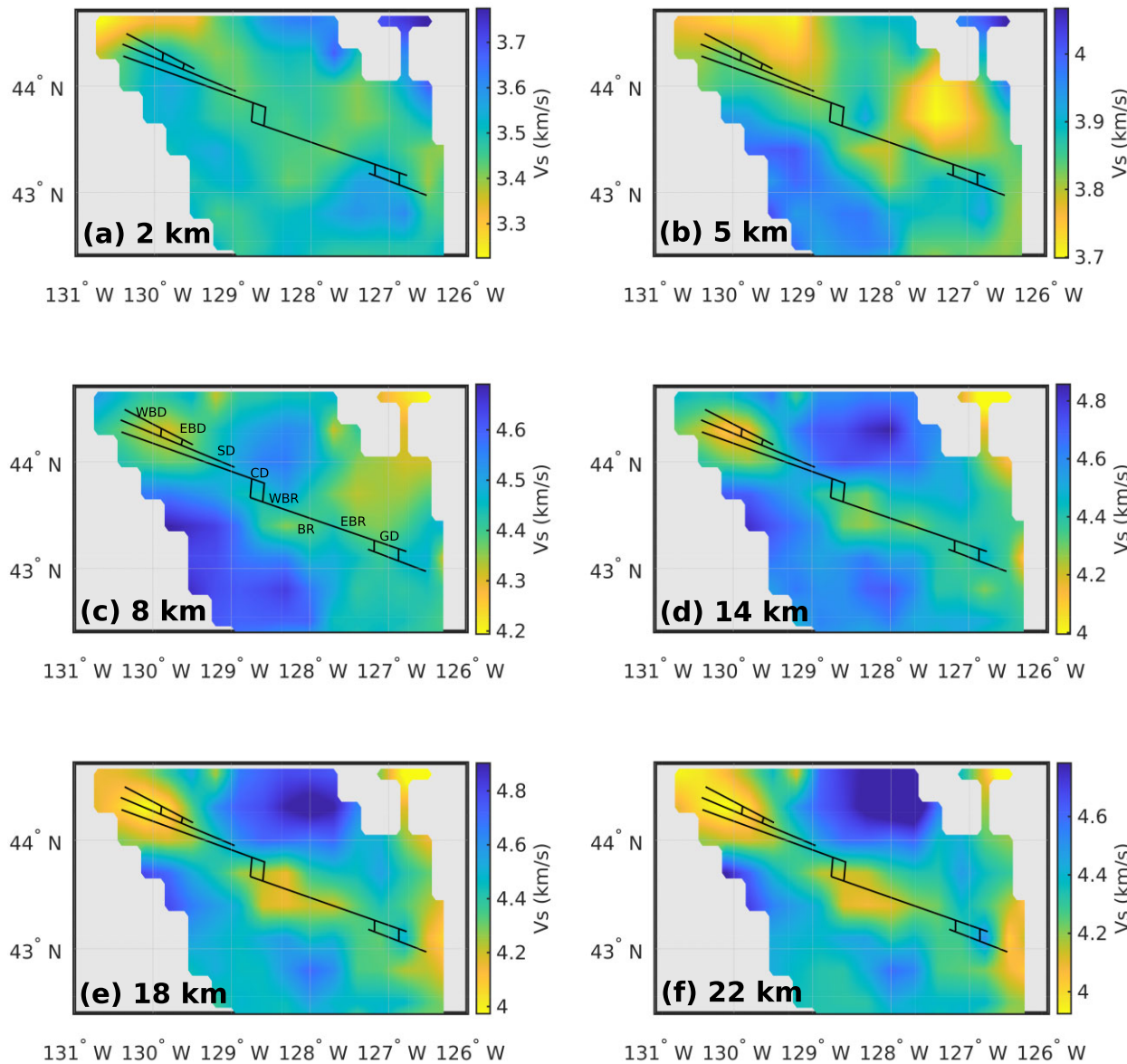


Figure 9. The estimated shear-wave velocity model at selected depths of 2, 5, 8, 14, 18 and 22 km. The model is computed as the mean of the ensemble of final models from the linearized iterative inversion. The segments of the BTFZ are shown in (c) as: WBD – Western Blanco depression, EBD – Eastern Blanco depression, SD – Surveyor depression, CD – Cascadia depression, WBR – Western Blanco ridge, BR – Blanco ridge, EBR – Eastern Blanco ridge and GD – Gorda depression.

two representative grid nodes (latitude: 43.4° , longitude: -127.7° and latitude: 43.1° , longitude: -126.8°) along the BTFZ. Uncertainties are remarkably large ($\sim 0.3\text{--}0.5 \text{ km s}^{-1}$) in the sediment layer (Figs 8b and d) where lack of short period dispersion measurements may have undermined their resolution. For this reason, in this study, we do not interpret velocities in the sediment layer and depth = 0 km in subsequent representations/manifestations of the shear-wave velocity model correspond to the top of the crust unless otherwise specified. At upper mantle depths of $\sim 24\text{--}30$ km, there is a relatively sporadic increase in standard deviation to over $\sim 0.1 \text{ km s}^{-1}$, indicating inconsistencies in the set of recovered models. This observation is strongly consistent with the depth sensitivity of our surface wave data (Fig. 7), thus, we conservatively only present shear-wave velocity structure from the crust to a depth of ~ 22 km.

The final 3-D shear-wave velocity model is obtained by compiling all 1-D shear-wave velocity profiles derived for every $0.3^\circ \times 0.3^\circ$ grid node. Horizontal sections of the 3-D shear-wave velocity model at six representative depths are displayed in Fig. 9 while their corresponding uncertainties are shown in Fig. S10. Uncertainties in the crust are fairly homogeneous (Figs S10a and b), ranging from around $10\text{--}60 \text{ m s}^{-1}$ and averaging about 30 m s^{-1} across the study region. At the shallowest mantle depths of $6\text{--}8$ km (Fig. S10c), uncertainties increase slightly, averaging about 50 m s^{-1} . Because the sensitivity of short period surface wave dispersion data decreases with increasing depth, uncertainties are larger and more variable at the deepest depths of $\sim \geq 18$ km (Figs S10e and f), reaching over 100 m s^{-1} at some locations (mostly within the Juan de Fuca Plate with limited raypath coverage; Fig. S11) with a mean of about 70 m s^{-1} across the study region.

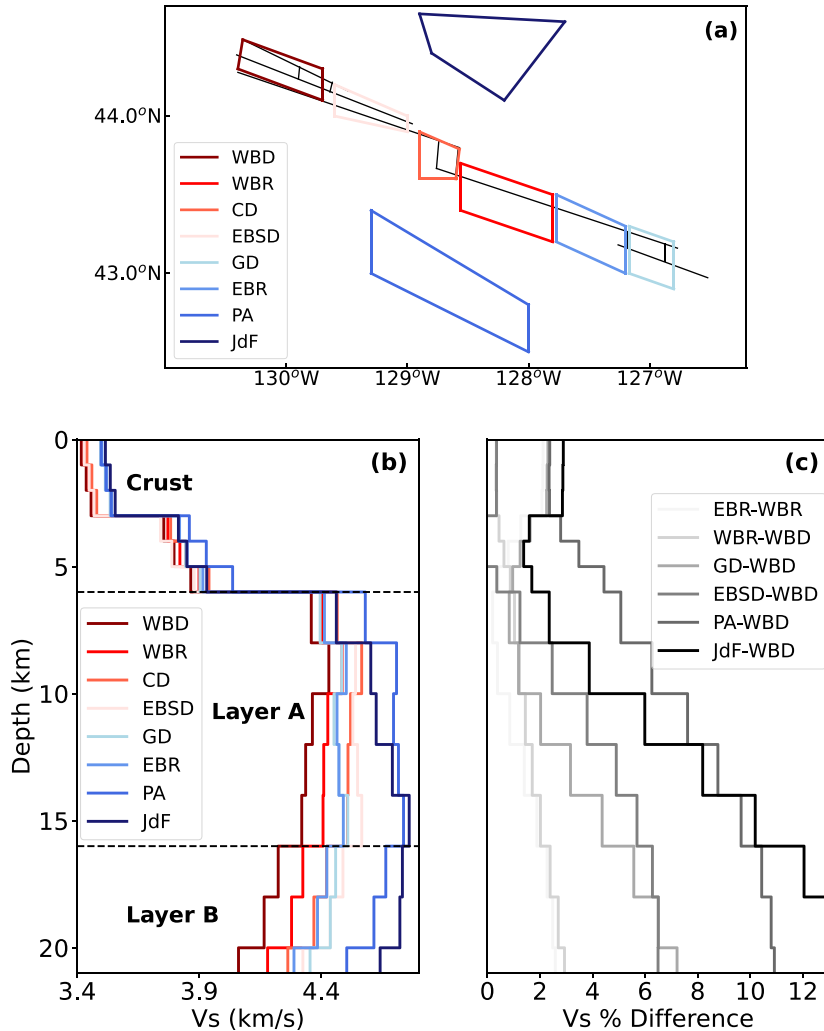


Figure 10. (a) Outline of the study area with areas used to calculate segment average 1-D V_s structures shown in coloured boxes. (b) Average 1-D V_s profiles calculated for the segments of the BTFZ (WBD, WBR, CD, EBSD, GD and EBR), Pacific Plate (PA) and Juan de Fuca Plate (JdF) boxed in (a). (c) Per cent shear-wave velocity difference between 1-D V_s profiles in (b). Note: Depth = 0 km corresponds to the top of the crust.

The shear-wave velocity model broadly shows variations similar to phase velocity which suggests robustness of the structural features. To help further illustrate observations in our shear-wave velocity model and compare structure beneath the different segments along the BTFZ, in Fig. 10, we show averages of the shear-wave velocity profile for six segments along the BTFZ, two off-axis regions and the differences between them. We also show seven vertical cross-sections of the velocity model, running along and across the strike of the BTFZ in Fig. 11. A summary of our shear-wave velocity model as horizontal slices from the crust to the maximum depth at intervals of 1 km in the crust and 2 km in the upper mantle is shown in Fig. S12. From the crust to uppermost mantle depths of up to ~ 22 km, in general, we observe slow shear-wave velocities that are sometimes segmented along the BTFZ (Figs 9, 11 and 12). In the shallow crust corresponding to the 2 km map (Fig. 9a), slow shear-wave velocities (~ 3.3 – 3.4 km s $^{-1}$) trend the inside corner of the BTFZ-Juan de Fuca RTI, northern boundary of western BTFZ and central BTFZ. Relatively faster velocities (~ 3.5 km s $^{-1}$) seen in western BTFZ may represent several topographic highs like PP that bound the western basins. Slow velocities are also observed at depths of ~ 4 – 8 km in a section of the Juan de Fuca Plate

adjacent to the eastern BR. Gao (2016) and Gao (2018) in a large-scale study of the Cascadia subduction system and VanderBeek & Toomey (2019) also imaged a similar feature at a depth of ~ 9 km and in the lithospheric mantle, respectively. Its location coincides with a pseudofault associated with the second of a series of ridge propagation events (Fig. 1) that culminated in the formation of the BTFZ (Wilson *et al.* 1984). Seismic reflection and gravity data (e.g. Calvert *et al.* 1990; Nedimović *et al.* 2008; Marjanović *et al.* 2011) have revealed pseudofaults flanking the Juan de Fuca ridge to be characterized by anomalous crustal structure and layer 2A thickness. In particular, along this propagator wake, VanderBeek & Toomey (2019) imaged both relatively fast and slow P -wave uppermost mantle velocities that suggest a variable structure beneath the fault characterized by distinct thermal and tectonic conditions. Consistent with Nedimović *et al.* (2008), we speculate that the reduced shear-wave velocity is possibly caused by localized and enhanced crustal shearing and fracturing which facilitate fluid infiltration and mineral alteration in the uppermost mantle. In the 5 km map, the slowest shear-wave velocities along the BTFZ (~ 3.8 – 3.9 km s $^{-1}$) are seen roughly around the central to western areas of the BR and the inside corner of the BTFZ-Juan de Fuca RTI, stretching along

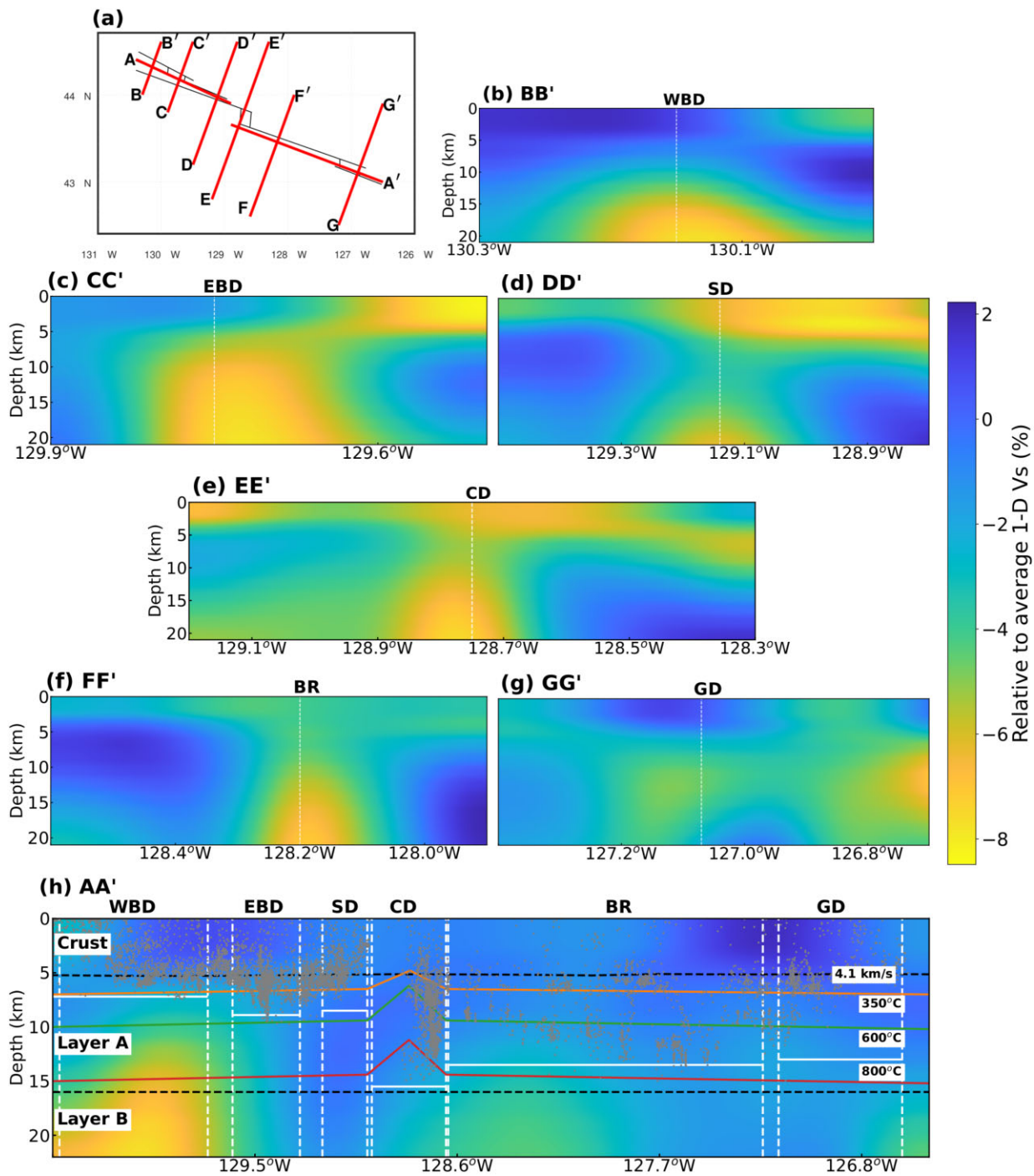


Figure 11. (b–h) Depth cross-sections running along the seven profiles (A–A', B–B', C–C', D–D', E–E', F–F', G–G') identified in (a). The vertical white broken lines in (b–g) indicate the approximate locations of the segments of the BTFZ. The horizontal white lines in (h) indicate the approximate maximum depth of seismicity in each segment (Kuna 2020; Ren *et al.* 2023). The 350 °C, 600 °C and 800 °C isotherms calculated from a numerical model considering hydrothermal cooling (Roland *et al.* 2010) are shown in (h). Seismicity distribution plotted as grey circles in (h) are from Kuna (2020).

the northern boundary of the WBD, EBD and SD. At this depth, slightly fast shear-wave velocities ($\sim 4 \text{ km s}^{-1}$) dominate the Pacific Plate and some portions of the Juan de Fuca Plate approximately opposite the CD. Amongst all six segment average shear-wave velocity profiles along the BTFZ (Fig. 10a), the WBD, eastern Blanco and Surveyor depressions (EBSD) and western Blanco ridge (WBR) are the slowest ($3.4\text{--}3.8 \text{ km s}^{-1}$) in the crust while the CD, eastern Blanco ridge (EBR) and GD are the fastest ($3.5\text{--}3.9 \text{ km s}^{-1}$).

At the uppermost mantle depth of 8 km (Fig. 9c), two distinct slow velocity zones ($\sim 4.3\text{--}4.4 \text{ km s}^{-1}$) are seen along the BTFZ at locations roughly corresponding to the WBD and EBD, and the central to westernmost BR. Similar shear-wave velocity variations but slightly slower ($\sim 4.1\text{--}4.2 \text{ km s}^{-1}$) are observed along the BTFZ at the $\sim 18\text{--}22$ km depths (Figs 9e, f and S12l–n). Here, the slow velocities along the BR appear to extend into the CD while velocities on the bounding Juan de Fuca and Pacific plates are generally faster

($\sim 4.6\text{--}4.8 \text{ km s}^{-1}$). Overall, the Juan de Fuca Plate appears faster than the Pacific Plate at depths $\sim 14 \text{ km}$ as also observed by Bell *et al.* (2016), Byrnes *et al.* (2017) and Wu *et al.* (2023). In the uppermost mantle along the BTFZ, shear-wave velocity variation reaches $\sim >7$ per cent (Fig. 10b) and exhibits negative gradient starting from a depth of $\sim 10 \text{ km}$ (Fig. 10a). At these depths, the WBD that is adjacent to the western RTI and WBR constitute the slowest segments. While the WBD is on average about 4 and 5 per cent slower than the GD that is located close to the eastern RTI and EBSD, respectively, the WBR is interestingly ~ 2 per cent slower than the EBR (Fig. 10b). To facilitate comparison with previous tomographic studies in the region, we have shown fairly resolved sections of the Gorda ridge that reveal the tectonic feature as a broad region of relatively slow velocities (see summary of our shear-wave velocity model in Fig. S12).

4.3 Comparison with previous studies

There have been some tomographic studies in the Cascadia subduction region encompassing the Juan de Fuca–Blanco–Gorda Plate system using data set from similar seismic stations as this study (e.g. Wagner *et al.* 2010; Porritt *et al.* 2011; Gao 2016, 2018; Byrnes *et al.* 2017; Rathnayaka & Gao 2017; Janiszewski *et al.* 2019; VanderBeek & Toomey 2019; Wu *et al.* 2023). Here, we briefly compare our study and results with the most recent ones of note. Gao (2016, 2018) obtained a 3-D shear-wave velocity model of the crust and upper mantle, spanning the Juan de Fuca and Gorda spreading centres to the Cascade back arc, using full-wave propagation simulation and joint inversion of ambient noise (fundamental mode Rayleigh waves; 7–50 s) and regional seismicity (10–100 s) data. These periods are mostly sensitive to the oceanic upper mantle shear-wave velocity structure ($\sim 9\text{--}75 \text{ km}$) which limits a direct and comprehensive comparison with our short period (4–8 s) results. At depths of 9, 14 and 22 km common to the studies, the BTFZ is relatively poorly constrained by Gao (2016) as observed in their checkerboard tests. Notwithstanding, we still observe some significant similarities in the variation of shear-wave velocity. In their 9 km maps [figs 2d and 3a in Gao (2016) and Gao (2018), respectively], a low velocity zone is imaged in the Juan de Fuca Plate, adjacent to the northern wall of eastern Blanco. It extends into the BTFZ-Gorda RTI and the northernmost to central parts of Gorda ridge in Gao (2016). We observe a similar feature at $\sim 4\text{--}8 \text{ km}$ (Figs 9a–c and S12b–i) but faster (difference of $\sim 0.5 \text{ km s}^{-1}$) at depths $\geq 8 \text{ km}$ in comparison with Gao (2016), and mostly focused within the Juan de Fuca Plate. The raypaths of the fundamental mode Rayleigh-waves in Gao (2016) traverse significant sections of the continental lithosphere, the accretionary wedge and the deep ocean (where the BTFZ is located) where depth sensitivity varies at periods of $\sim 10 \text{ s}$. For instance, using starting models that consist of true water depths and sediment thicknesses, at 10 s period, depth sensitivity peaks at ~ 15 , ~ 5 and $\sim 12 \text{ km}$ in the continent, accretionary wedge and deep ocean, respectively. This implies that the average velocity of the medium between seismic stations in, say, the accretionary wedge and the deep ocean is influenced by the slower crustal structure of the accretionary wedge and the faster uppermost mantle structure in the deep ocean. We, thus, believe that the shear-wave velocities in the vicinity of the BTFZ at $\sim 9 \text{ km}$ in Gao (2016) and Gao (2018) may have been significantly slowed by multiple raypaths that traverse the slower accretionary wedge and continental crust across the Cascadia deformation front. At the 14 and 22 km depths (figs 2e and f in Gao 2016) where our maps (Figs 9d and

f) show the slowest velocities red ($\sim 4\text{--}4.2 \text{ km s}^{-1}$) beneath western and central Blanco, Gao (2016) also observed similarly slow velocities ($\sim 4\text{--}4.4 \text{ km s}^{-1}$). However, at 22 km where we observed slow velocities beneath the WBR ($\sim 4.1 \text{ km s}^{-1}$; Fig. 9f), Gao (2016) have imaged faster velocities ($\sim >4.5 \text{ km s}^{-1}$) that extend throughout eastern Blanco. It is important to note that Gao (2016, 2018) did not utilize data from 30 seismic stations of the Blanco experiment used in our study which have provided more local constraints, facilitating a more accurate imaging of structures beneath the BTFZ. In the most recent study over the region, Wu *et al.* (2023) developed a 3-D shear-wave velocity model of the region from fundamental mode Rayleigh-wave measurements (10–80 s). At their shallowest depth range of 20–40 km (fig. 7b in Wu *et al.* 2023), the BTFZ and Gorda ridge are revealed as regions of slow velocities broadly in agreement with our results (Figs 9e and f). VanderBeek & Toomey (2019) inverted Pn traveltimes for P-wave velocity structure of the uppermost mantle beneath the Pacific northwest. Generally consistent with our results (Figs 9d–f and S12g–n), they imaged the uppermost mantle beneath the BTFZ and Gorda ridge as relatively slow velocities. Another study by Bell *et al.* (2016) used fundamental mode Rayleigh waves extracted from teleseismic earthquakes in the period band 20–143 s to model the shear-wave velocity structure of the upper mantle beneath Juan de Fuca and Gorda plates. The lack of short period ($<10 \text{ s}$) surface wave measurements restricted their study to greater than 24 km depth. At 25 km depth, they obtained the Gorda ridge as a low velocity zone ($\sim 4.1 \text{ km s}^{-1}$) broadly akin to our observation in the uppermost mantle (Figs S12g–n). Other tomographic studies in the Cascadia region have either not geographically covered the entire BTFZ and/or focused on the deeper ($>30 \text{ km}$) mantle structure (e.g. Wagner *et al.* 2010; Porritt *et al.* 2011; Byrnes *et al.* 2017; Rathnayaka & Gao 2017), thus, limiting comparison with our results. Overall, at overlapping periods and depths, there is a fairly good agreement between our observations and those from previous studies. The few observed differences can be attributed to a number of factors that include the use of different inversion methods, data types and station distribution.

5 DISCUSSION

5.1 Causes of slow velocities along the BTFZ

To interpret the reduced seismic velocities ($\sim 0.2\text{--}0.45 \text{ km s}^{-1}$; $\sim 4\text{--}8$ per cent) we observe along the BTFZ from crust to uppermost mantle depths of $\sim 22 \text{ km}$, it is important to first consider the mechanisms and types of material variations that are likely responsible. We note here that significant lateral smoothing has been applied to the tomographic inversions, and therefore, the true fault zone rocks should have even slower seismic velocities within a narrower zone than we have imaged. This makes our results a lower bound on the magnitude of possible velocity reduction. Previous studies of continental and oceanic strike-slip faults have identified intense fracturing (e.g. Tréhu & Purdy 1984; Chester *et al.* 1993; Van Avendonk *et al.* 1998, 2001; Roland *et al.* 2012) and mineral alteration (e.g. Bonatti 1978; Detrick *et al.* 1982; White *et al.* 1984; Detrick *et al.* 1993; Faulkner *et al.* 2003) as the two most likely factors responsible for the significantly reduced slow velocities observed within the broad transform deformation zone. Globally, abundant seismicity has been reported along OTFs (McGuire *et al.* 2012; Wolfson-Schwehr & Boettcher 2019; Kuna 2020; Yu *et al.* 2021), especially within the typical oceanic crustal

Layer 3 that extends from ~ 2 km beneath the ocean floor to the Moho. Slip during an earthquake induces brittle deformation in the broad transform fault zone that creates and sustains highly permeable pathways for seawater infiltration, leading to enhanced crustal hydration that can be imaged as slow velocities. For example, in the East Pacific Rise (EPR), alongside evidence from gravity data and effective media analysis, Roland *et al.* (2012) interpreted the slow velocities imaged along the Gofar and Quebrada transform faults at depths of ~ 3 – 9 km as dominantly due to intense fracturing. Also along the EPR, Van Avendonk *et al.* (2001) attributed the anomalously low compressional velocities from seafloor to the Moho to intense brittle deformation caused by transpression along the transform plate boundary. Similarly, in the Atlantic, extensive fracturing and faulting were invoked by White *et al.* (1984) to explain the upper crustal slow velocities imaged in Kane, Vema and Oceanographer.

Until recently, the depth extent of brittle deformation along OTFs has been a topic of intense debate. Although some earlier studies (e.g. McKenzie *et al.* 2005; Abercrombie & Ekström 2001) have suggested a cut-off depth corresponding to the ~ 600 °C isotherm, microstructural and textural analysis of peridotite mylonites recovered from Shaka, Prince Edwards and Romanche OTFs (Kohli & Warren 2020; Prigent *et al.* 2020), alongside recent records of deep OTFs seismicity [extending beyond and reaching depths corresponding to the ~ 600 °C and >1000 °C isotherms, respectively; Kuna *et al.* (2019); McGuire *et al.* (2012); Wolfson-Schwehr *et al.* (2014)], indicate fluid infiltration and brittle to semi-brittle fracturing deep into the ductile upper mantle parts of OTFs. These conditions are expected to facilitate fluid-rock interactions that may result in serpentinization of mantle peridotite and/or formation of mylonitic peridotites that will affect the structural, compositional and mechanical properties of OTFs and, invariably, reduce seismic velocities. Just as observed for other OTFs, especially in the Atlantic, at upper mantle depths from the Moho to ~ 16 km in Romanche TF, Wang *et al.* (2022) obtained around ~ 12.4 per cent reduction in seismic velocity which they interpreted as being caused by the serpentinization of mantle peridotite. The presence of small amount of partial melts at upper mantle depths have also been occasionally invoked to explain slow velocities along OTFs (Wang *et al.* 2022).

The sharpest velocity contrasts in the average shear-wave velocity profiles along the BTFZ (Fig. 10a) are observed at depths of ~ 6 km (corresponding to the Moho) and ~ 16 km in the uppermost mantle. On average, in the crust, the vertical velocity gradient is ~ 83 m s $^{-1}$ km $^{-1}$.

It reduces drastically to ~ 10 m s $^{-1}$ km $^{-1}$ at depths just below the Moho to ~ 16 km and becomes negative (~ -50 m s $^{-1}$ km $^{-1}$) at the deepest depths from ~ 16 to 22 km. Based on these variations in shear-wave velocity in our models (Figs 9, 10 and 11h), predicted thermal structure of the BTFZ considering hydrothermal circulation in the shallow lithosphere (Roland *et al.* 2010) and petrological constraints from OTFs, we divide the BTFZ into three depth ranges and suggest possible causes for their respective slow velocity anomalies. Here, we define the crust to extend from the seafloor to the Moho at ~ 6 km which is roughly constrained by the ~ 350 °C isotherm (Fig. 11h), representing the lower stability limit of antigorite (Ji *et al.* 2013). Low-temperature serpentine (lizardite and chrysotile) are stable at temperatures $\sim <350$ °C (Ji *et al.* 2013) and exhibit significantly reduced density relative to unaltered mafic rocks. This should result in anomalously reduced gravity observations not accounted for by bathymetry which is not observed along the BTFZ (Sandwell *et al.* 2014) just as in Gofar and Quebrada in the EPR (Roland *et al.* 2012). As such, we interpret the crustal slow

velocities (~ 3.3 – 3.9 km s $^{-1}$) to be dominantly due to extensive fracturing and hydration that result in fluid-filled pores, and possibly a small component of mineral alteration at the base of the crust. Relatively hot and young basaltic rocks in the vicinity of the RTIs may also explain crustal slow velocities.

We further divide the uppermost mantle into two layers: (i) Layer A, from the Moho to 16 km depth where there is a relatively sharp change in shear-wave velocity across all segments of the BTFZ (Fig. 10a) and that is approximately constrained by temperature range of ~ 350 – 700 / 800 °C (Fig. 11h) and (ii) Layer B, from depth of 16 km constrained approximately by the ~ 700 / 800 °C isotherm (that roughly represents the upper thermal stability limit of antigorite (Ji *et al.* 2013)) to the maximum depth of ~ 22 km (Fig. 11h). Abundant seismicity located at the shallowest depths (~ 6 – 10 km) within Layer A along the BTFZ (Kuna 2020; Ren *et al.* 2023) can create and sustain pathways for deep hydrothermal circulation that results in the alteration of uppermost mantle rocks. Considering that serpentinization occurs over a wide range of temperature (~ 350 – 700 °C and even higher temperatures in the presence of a small amount of aluminium; Ji *et al.* (2013); Bromiley & Pawley (2003)) consistent with these depths, we interpret the slow velocities in Layer A as mostly due to serpentinized mantle peridotite and/or the deformation (brittle and/or ductile) of the uppermost mantle. Although there is no record of serpentinites dredged from the BTFZ whose petrology is scantily known, a mylonite block was recovered along its eastern half during a dive series in 1994 (Dziak *et al.* 2000), indicating deep fluid-rock interactions.

At depths corresponding to temperatures above ~ 700 / 800 °C isotherm consistent with our Layer B, the thermal stability limit of serpentine group minerals is perhaps exceeded (Ji *et al.* 2013). Slow velocities observed at these depths (Figs 9 e and f) are likely due to high temperature mylonitization caused by deeper extent of fluid infiltration and/or the presence of partial melts. Observations of seismicity extending to upper mantle depths corresponding to temperatures > 600 °C (Wolfson-Schwehr *et al.* 2014; Kuna *et al.* 2019) suggest a deeper depth for the transition from brittle to ductile deformation than earlier thought. Episodes of brittle deformation at these depths along the BTFZ can create short-lived cracks that enhance and drive the penetration of seawater-derived fluids to deeper depths. This facilitates hydration reactions that likely lead to the formation of hydrated mylonitic peridotites as in Romanche (Wang *et al.* 2022) in Layer B. The temperature range of ~ 850 – 950 ± 50 °C which falls within this layer has been estimated for the development of hydrated mylonites (Drury *et al.* 1991; Prigent *et al.* 2020). Also, in the presence of water at a temperature of ~ 920 °C, the mantle will melt. Volcanic activities in the vicinity of the RTIs in Blanco, which have been inferred from dredged basaltic glass (Duncan 1968), may also explain the slow velocities at these depths. Mantle upwelling has also been proposed to be widespread beneath OTFs based on observations of mostly near vertical symmetry axis from shear-wave splitting measurements (Eakin *et al.* 2018).

5.2 Porosity, serpentinization, hydration, mylonitization and melt fraction estimates

To evaluate the degree of fracturing and quantitatively estimate the resulting porosity that can explain the slow velocities we observe within the crust along the BTFZ, we perform effective media analyses assuming fluid-saturated porosity. Some theoretical models (Wu 1966; Walsh 1969) and experimental data on porous rocks (Nur & Simmons 1969) show that their effective elastic moduli

and velocities depend strongly on the shape of the inclusions represented by their aspect ratios (α), which are generally not well constrained. First, we compute and show the Hashin-Shtrikman (HS) upper and lower bounds (Hashin & Shtrikman 1963) on the shear-wave velocity for seawater-filled composite of basalt/gabbro in the crust over a range of porosities (shaded region in Fig. 12a), representing a wide spectrum of possible pore geometries. The model of Kuster & Toksöz (1974) considered the effects of different fracture geometries on the seismic wave velocities associated with porosity. We implement this model to estimate the elastic moduli and shear-wave velocity for the composite medium as a function of pore concentration, considering crack-like fractures similar to those that have been observed along continental strike-slip faults (Savage & Brodsky 2011). For all pore geometries shown as coloured curves in Fig. 12a, shear-wave velocity decreases with increase in porosity and all curves fall within the HS bounds. Conservatively assuming oblate spheroidal pores with aspect ratios, α , ranging from 5 to 100 (curves in Fig. 12a), the slowest velocities (~ 3.4 – 3.9 km/s) we observed within the crust along the BTFZ are consistent with porosity values of ~ 10.9 per cent just below the seafloor to ~ 0.4 per cent at the crust-uppermost mantle boundary.

Lizardite and chrysotile, the low-temperature (LT) serpentines are only stable at temperatures below $\sim 350^\circ\text{C}$ (Evans 2004) while

Antigorite, the high-temperature (HT) form is stable over a wide temperature range of up to ~ 700 – 800°C (Ji *et al.* 2013). Accordingly, HT serpentinization is expected to be present in Layer A. Ji *et al.* (2013) have provided an experimental relationship between seismic velocities and degree of serpentinization:

$$V_s = 4.51 - 0.84\phi_{HT}, \quad (2)$$

where V_s is the shear-wave velocity and ϕ_{HT} is the serpentine volume fraction. In Layer A (6–16 km; 6 km depth excluded), we observe shear-wave velocities of ~ 4.2 – 4.5 km/s along the BTFZ. Using eq. (2), these shear-wave velocities are consistent with ~ 1.2 – 37 vol per cent (0.13– 4.0 wt per cent) of HT serpentinization. Thus, Layer A is characterized as a ~ 10 km-thick, partially serpentinized uppermost mantle layer.

In Layer B (16–22 km depth), since the thermal stability of the serpentine group minerals is likely exceeded, the slow velocities may be explained by high-temperature mylonitization and/or the presence of partial melts. The shear-wave velocity variation for increasing amount of hydrous phases in Layer B is estimated using an effective medium analysis (Eshelby 1957; Berryman 1992; Taylor & Singh 2002). See Text S1 in the Supporting Information for details. Melt-impregnated peridotite is assumed to be the dominant peridotite at these depths as found in Romanche (Tartarotti *et al.* 2002), comprising of approximately 58.8 per cent olivine,

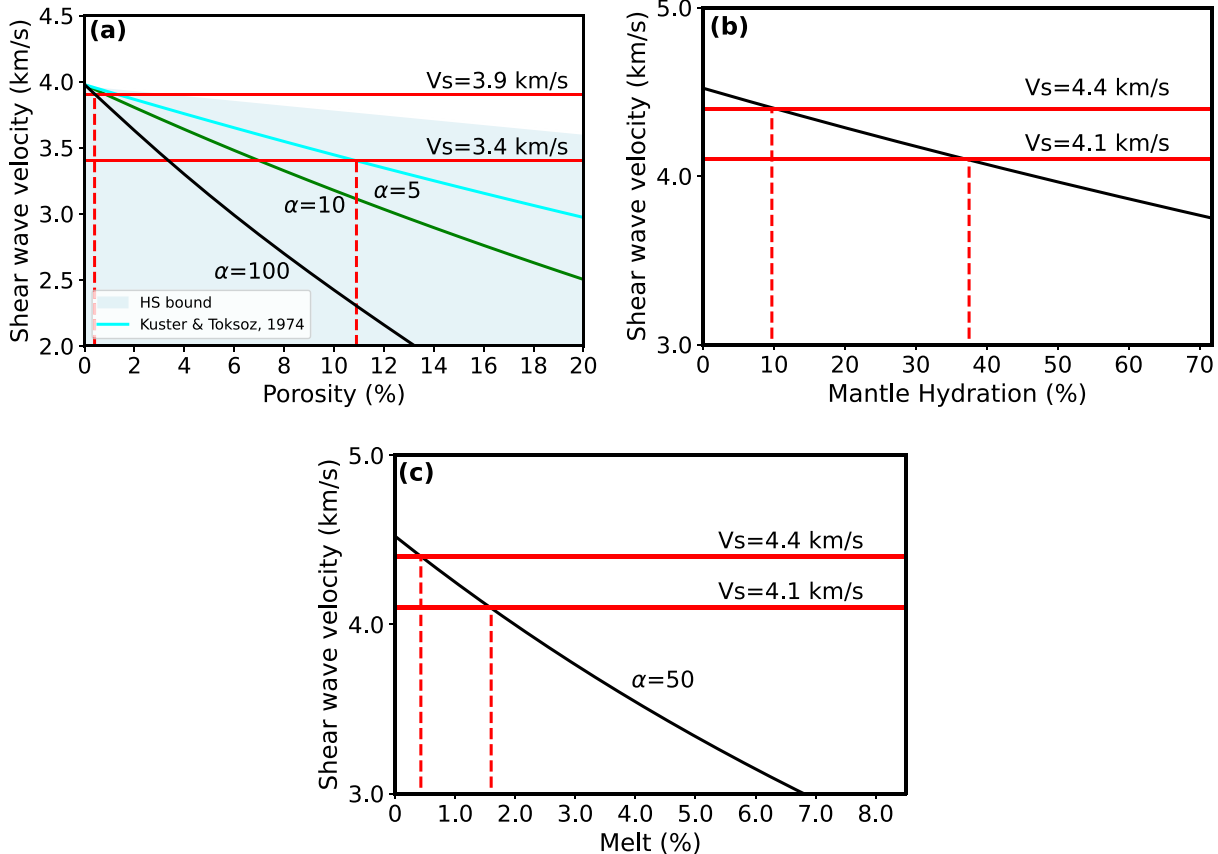


Figure 12. (a) Effective media analyses assuming fluid-filled porosity in the crust along the BTFZ. Seismic shear-wave velocity variation with respect to seawater-saturated porosity in basalt/gabbro is computed using the Hashin-Shtrikman (HS) mixing relations (shaded region) and the two-phase media relations of Kuster & Toksöz (1974), considering oblate spheroidal pores with aspect ratios (α) = 5, 10 and 100. Elastic moduli of the constituent rock minerals are obtained from Carlson & Miller (2004). (b) Shear-wave velocity in Layer B as a function of degree of hydration. (c) Shear-wave velocity as a function of melt fraction in Layer B using aspect ratio of melt, $\alpha=50$. The solid red lines indicate the upper and lower bounds of shear-wave velocity in the respective layers along the BTFZ.

7.45 per cent orthopyroxene, 23.85 per cent clinopyroxene, 1.6 per cent spinel and 8.3 per cent plagioclase. Elastic moduli of the different minerals are obtained from Collins *et al.* (1989), Carlson & Miller (2004) and Abers & Hacker (2016) as shown in Table S2 in the Supporting Information, and used for our calculations, revealing that ~9.7–37.5 per cent amphibole is required to account for shear-wave velocities of ~4.1–4.4 km/s in Layer B (Fig. 12b). Based on natural sampled high-temperature peridotite mylonites from Shaka and Prince Edward OTFs, comprising of ~12.5 per cent amphiboles (Prigent *et al.* 2020), our calculated degree of hydration implies that ~>77 per cent of Layer B is mylonitic. We note that grain size reduction accompanying mylonitization would lead to strain localization (Bickert *et al.* 2023) and additional decrease in the shear-wave velocities, thereby, making our estimates of uppermost mantle hydration the upper bounds. Considering that a ~77 per cent degree of mylonitization is quite high, the slow velocities at these depths may be attributed to a combination of two or more physical mechanisms. Although mylonites have been recovered from the BTFZ (Dziak *et al.* 2000), there are no available records of their analysis.

Several studies have interpreted the shear-wave velocity decrease at the base of the oceanic lithosphere to indicate the lithosphere–asthenosphere boundary (e.g. Burgos *et al.* 2014; Harmon *et al.* 2020). Similarly, the velocity drop we have observed in Layer B (Fig. 10b) suggests the beginning of the lithosphere–asthenosphere boundary, and thus possibly the presence of melt. If the presence of partial melts is dominantly responsible for the reduced velocities in Layer B, the fractions of partial melt that can explain the low shear-wave velocities (4.1–4.4 km/s) are estimated using the differential effective medium theory (DEM) (Taylor & Singh 2002). We use the same composition of melt-impregnated mantle peridotites as in the degree of hydration computation. The density, shear and bulk moduli of melt are obtained from Clark *et al.* (2016). Assuming the melt inclusions are oblate spheroids with aspect ratio of 50 as adopted by Wang *et al.* (2022) in Romanche, the estimated melt fractions in Layer B that can explain the imaged slow velocities fall in the range of ~0.43–1.6 per cent (Fig. 12c).

5.3 Crustal accretion along OTFs

We observe the slowest crustal velocities along the BTFZ in the vicinity of the Blanco-Juan de Fuca RTI, extending into the WBD (Figs 6a,b, 9a and b). This is consistent with intense deformation and the presence of multiple fractures and cracks due to regional strain. Weakly deformed lavas, breccias and dolerites have been observed and dredged from the north and south walls of the westernmost ~40 km of the BTFZ (Melson 1969; Karson *et al.* 2002). The overshooting Juan de Fuca ridge tip that appears to slightly extend over the RTI into the transform fault (Fig. 1) indicates continuation of the magma chamber that feeds the westernmost segment of the transform fault (Stakes *et al.* 2006; Ren *et al.* 2023). Similar observations have been made in the Sequeiros OTF where the ridge tips also form magma rich J-shaped abyssal hills (Fornari 1989). This appears to be consistent with the imaged uppermost mantle slow shear-wave velocities (~4.1–4.3 km/s; Figs 9e,f and 10a) in Layer B in the westernmost BTFZ, which can be explained by the presence of up to 1.6 per cent partial melt (Fig. 12c) that extends into Layer A at some locations. Similarly slow shear-wave velocities (~4.1 km/s) in the uppermost mantle (~10–30 km) consistent with partial melt fraction somewhat smaller than 1 per cent have earlier

been reported in the Juan de Fuca Plate, ~15 km away from the ridge axis (Tian *et al.* 2013).

The small patch of slow shear-wave velocities (~4.1 km/s) in Layer B adjacent to the Blanco-Gorda RTI (Fig. 11h) suggests a smaller volume of magma supply to the transform fault compared to at the Blanco-Juan de Fuca RTI. At these uppermost mantle depths, the WBD is over 6 per cent slower than the GD (Fig. 10b). Bathymetry along both ridge axes (Fig. 1) provides further support for this inferred difference in magma supply. Compared to the Juan de Fuca ridge axis marked by bathymetric high that suggests abundant magma upwelling, the Gorda ridge axis is marked by bathymetric low similar to magma starved slow-spreading centres in the Atlantic. In addition, while the J-shaped ridges appear to extend into the transform valley at the Blanco-Juan de Fuca RTI, they are truncated at the Blanco-Gorda RTI. Nonetheless, the presence of basaltic glass in cores near the Blanco-Gorda RTI suggests recent submarine volcanism (Duncan 1968). Also, in 1996, its northernmost segment was the site of a small volume eruption (Clague *et al.* 2020). Overall, the observed disparity in uppermost mantle seismic velocities (especially in Layer B) indicate varying degrees of magmatism at both RTIs consistent with magma supply at corresponding proximal ridge segments inferred from seafloor bathymetry.

Fox & Gallo (1984) proposed that magmatic crust formed at the RTI and emplaced in its inside corner propagates along the transform fault zone unmodified before becoming part of the fracture zone. Seismicity studies (e.g. Engeln *et al.* 1986; Abercrombie & Ekström 2001) have located predominantly strike-slip earthquakes along OTFs, consistent with their conventional characterization as two-dimensional strike-slip plate boundaries where the lithosphere is neither created nor destroyed while it cools and deepens as a function of the age of the plate. Lately, with increasing number of studies on global OTFs, this simple characterization has received some pushbacks. Firstly, in an analysis of global high-resolution multibeam bathymetry data of OTFs that included all possible slipping rates, Grevemeyer *et al.* (2021) observed fracture zones to be systematically shallower than their parent transform faults by ~1.6 km, contradicting plate-cooling arguments. With numerical modelling, they explained this observation by proposing a two-stage accretion process taking place at both RTIs separated in time by a period of horizontal extension that thins the lithosphere as it propagates along the transform fault. High-resolution 3-D seismic observations of fracture zones in São Tome and Príncipe, eastern Gulf of Guinea presented by Thomas *et al.* (2022) broadly support conclusions of this numerical model. They observed thinned complex intra-transform structures associated with extrusive lava flows and extensional transform processes that were covered by lavas derived from trailing ridge segments. Based on tomographic inversion of seismic refraction and wide-angle data collected for the St. Paul fracture zone in the equatorial Atlantic ocean, Growe *et al.* (2021) observed near-normal oceanic crust (~5–6 km) and uppermost mantle ($V_p = 8$ km/s) along the fracture zone that may indicate a second stage of magmatic addition at the proximal RTI as proposed by Grevemeyer *et al.* (2021) before becoming part of the fracture zone. In western Blanco, our results can be explained by the presence of up to 1.6 per cent partial melt in the upper mantle within the vicinity of the RTI that extend ~40 km into the transform valley. Because the solidus of dry mantle (~1400°C; Katz *et al.* (2003)) is much higher than the predicted temperature of ~800–1000°C in Layer B (upper mantle depth of 16–22 km) within the transform fault zone (Fig. 11h), the presence of water and/or carbon dioxide is

necessary to facilitate the formation of melt at these depths. Since the mantle is known to melt in the presence of water at a temperature of $\sim 920^\circ\text{C}$, the partial melt in Layer B within the vicinity of the RTIs is likely water induced. In Romanche TF, Wang *et al.* (2022) similarly interpreted the slow velocities at depths corresponding to temperatures of $\sim 900\text{--}1300^\circ\text{C}$ ($\sim 32\text{--}60$ km) as due to the presence of small amounts of water-induced partial melt. Compared to eastern Blanco that hosts several $M_w > 6$ earthquakes and whose crust is characterized by b-value of ~ 0.7 (Kuna 2020), western Blanco is dominated by small magnitude earthquakes (average b-value > 1 ; Kuna (2020)) that are less capable of creating and sustaining pathways for deep seawater infiltration. This suggests a relatively shallower extent of seawater infiltration in this region which is corroborated by its relatively faster crustal velocity (Fig. 11h). Based on the foregoing, the likely source of water in the vicinity of the western RTI is the sublithospheric water-bearing melt at the southernmost section of the Juan de Fuca ridge that migrated into the transform fault zone via deep horizontal flux (Keller & Katz 2016) and ascended into the lithospheric mantle. Beneath ridge axis, horizontal flux is achieved through corner flows (Hirschmann 2010; Mehouchi & Singh 2018) which may have been complemented by extensional shear zones at depths in the vicinity of the RTIs (Grevenmeyer *et al.* 2021) and active plate boundary reorganization in the younger western BTFZ (Braunmiller & Nábělek 2008; Ren *et al.* 2023) characterized by parallel to subparallel multi-strand transform faults similar to what has been suggested in Quebrada (Gong *et al.* 2022). In conjunction with evidence from bathymetric data, our tomographic observations at Blanco's RTIs can be explained by water-induced melting facilitated by lateral flux of sublithospheric water-bearing melts from the adjacent Juan de Fuca ridge segment.

Beneath the CD, at uppermost mantle depths of $\sim > 16$ km corresponding to Layer B, we observed similarly slow shear-wave velocities of ~ 4.2 km/s (Figs 9e,f, 11e,f and h) as within the RTIs, which can be explained by the presence of ~ 1.1 per cent partial melt (Fig. 12c). This is consistent with the observation of deep seismicity reaching depths of ~ 15 km beneath the CD interpreted to be likely due to rapidly cooled intermittent dike intrusions into the seismogenic lithosphere (Kuna 2020), which suggests the presence of a deep magma source beneath the region. The observed slow velocities can alternatively be explained by uppermost mantle hydration. However, this would imply water content of $\sim > 11.76$ wt per cent ($\sim > 77$ per cent mylonitization) in Layer B which is significantly higher than the water content of ~ 0.75 wt per cent (~ 7.0 per cent serpentinization) in Layer A. Therefore, we interpret the slow velocities in Layer B beneath the CD to be likely due to the presence of decompression induced partial melts as opposed to uppermost mantle hydration. Similarly slow velocities in Layer B beneath the adjacent WBR suggest the presence of partial melt that potentially migrated from the CD.

5.4 Seawater infiltration and seismicity distribution along the BTFZ

OTFs and their fracture zones that are ubiquitous along the ocean floor are important components of the hydrologic cycle. In short, they are believed to be regions where large volumes of seawater transmit into the lithosphere, modulating the pore pressure and effective normal stresses, cooling the lithosphere, and interacting with

surrounding rocks which could lead to drastic changes in the rheology of the oceanic lithosphere (Hensen *et al.* 2019). However, the depth extent and along-strike variability of fluid infiltration beneath global OTFs have remained unknown. In contrast, seismicity distribution have been relatively well observed along many OTFs, especially in the EPR (Gong & Fan 2022; Gong *et al.* 2023) and equatorial-Atlantic ocean (Yu *et al.* 2021; Schlaphorst *et al.* 2023). A recent one-year-long local seismological experiment along the BTFZ (Nabelek & Braunmiller 2012) located ~ 8000 earthquakes with local magnitude (ML) ranging from 0.6 to 5.5 (Kuna 2020). Earlier studies (e.g. Dziak *et al.* 1991; Braunmiller & Nábělek 2008) reported the BTFZ to be seismically very active with more than ten large shallow earthquakes of moment magnitude (M_w) ≥ 6 . They are nearly periodic, rupturing mostly two major asperities along the BR, separated by a barrier region of ~ 10 km approximately every 14 years (Boettcher & McGuire 2009). Although strike-slip motion (~ 96 per cent of all mechanisms; Kuna (2020)) overwhelmingly dominates the BTFZ, it is characterized by complex patterns of slip modes and seismicity distribution. These have been linked to the along-strike variation in fault zone material properties as in the EPR (Roland *et al.* 2012), influenced by the lateral and depth extent of hydrothermal circulation, degree of mineral alteration, magmatism, etc. In the subsequent subsections, we explore these relationships along different segments of the BTFZ using our seismic velocity models. We note that the resolution of our tomographic maps restrict a direct and detailed comparison with the fine-scale ($\sim < 5$ km) earthquake generation behaviour and seismicity distribution along the BTFZ (Kuna *et al.* 2019; Kuna 2020; Ren *et al.* 2023), especially in the western half that comprise of small pull-apart basins (Braunmiller & Nábělek 2008). Consequently, we focus on a macroscale picture of slip behaviour and seismicity distribution along the transform fault.

5.4.1 Western BTFZ

In the uppermost ~ 4 km of the crust, some of the slowest shear-wave velocities ($\sim 3.4\text{--}3.6$ km/s) along the BTFZ are observed in the western half, comprising of the WBD, EBD and SD (Figs 10a). They are consistent with $\sim > 2.5$ per cent water-saturated porosity (Fig. 12a), indicating relatively strong hydrothermal circulation in the crust. This can be explained by Western Blanco being the younger half of the BTFZ, believed to be currently undergoing plate boundary reorganization (Braunmiller & Nábělek 2008; Ren *et al.* 2023), which should result in highly fractured and permeable materials that enhance hydrothermal cooling. Fluid-filled porosity has been demonstrated to weaken fault zones (Okazaki *et al.* 2021), with strong dilatancy strengthening that stabilizes along-strike seismic rupture propagation hence favouring aseismic slip behaviour. Together with the relatively short lengths of the individual segments, this potentially reduces the tendency for the occurrence of large crustal earthquakes in western Blanco. This is consistent with the large seismic deficit of western Blanco (low seismic coupling of ~ 15 per cent; (Braunmiller & Nábělek 2008)) and the earthquakes being predominantly of small magnitudes with an average b-value of > 1 (Kuna 2020).

The relatively faster shear-wave velocities ($\sim \geq 4.5$ km/s; Fig. 10a) in the uppermost mantle (Layer A), especially beneath the SD are interpreted as due to $\sim \leq 1.2$ vol per cent degree of serpentinization, suggesting relatively limited fluid content. A lack of large crustal earthquakes capable of opening pathways for deep

seawater infiltration by rupturing into the uppermost mantle may have prevented deep extent of strong hydrothermal circulation at these segments. The western BTFZ hosts mostly crustal seismicity (not exceeding depths of $\sim 8\text{--}9$ km constrained roughly by the $\sim 600^\circ\text{C}$ isotherm predicted by the hydrothermal cooling model of Roland *et al.* (2010)) (Kuna 2020). Overall, these observations support shallow (~ 8 km) extent of seawater infiltration that is strongly connected with the maximum depth of seismicity within the western BTFZ.

5.4.2 Blanco ridge and Gorda depression

Some of the slowest seismic velocities in our tomographic models from crust to uppermost mantle depths are observed beneath the BR (Figs 9, 11 f and h), suggesting a strong and deep hydrothermal circulation beneath the fault segment. Crustal rocks dredged from the BR and GD show evidence of seawater-derived fluid infiltration (Hart *et al.* 1990). Compared to western BTFZ, the uppermost crustal shear-wave velocity in the BR is slightly slower ($\sim 3.4\text{--}3.5$ km/s) and consistent with fluid-filled porosity of $\sim >3$ per cent. The crust beneath the ~ 150 -km-long BR is almost seismically fully coupled (Braunmiller & Nábělek 2008; Kuna *et al.* 2019). Having a b-value of 0.78 (Kuna *et al.* 2019), it hosts the largest earthquakes ($\sim \geq \text{Mw } 6.0\text{--}6.4$) along the BTFZ (Boettcher & McGuire 2009; Kuna *et al.* 2019), creating and maintaining pathways for strong seawater infiltration into the uppermost mantle. The variation of shear-wave velocity along the BR reveals an apparent dichotomy between the western to central and easternmost parts of the fault segment (Figs 9d–f, 11h and Fig. S12g–n in the Supporting Information). The western to central region is relatively slower than the easternmost by up to ~ 2 per cent in the crust and Layer B, and ~ 1.3 per cent in Layer A (Fig. 10). This seems consistent with seismicity distribution along the fault segment. The western to central region (asperity at $\sim 128^\circ\text{W}$; Boettcher & McGuire (2009)) hosts the largest crustal earthquakes ($\sim \geq \text{Mw } 6.3\text{--}6.4$) (Boettcher & McGuire 2009) which should result in a higher degree of porosity that can enhance deep hydrothermal circulation. Also, large events in the eastern segment rupture preferentially towards the northwest into the western part (Braunmiller & Nábělek 2008). While in the western to central region, seismicity is consistent with a vertical fault cutting through the lithosphere, in the easternmost region, approximately east of $\sim 127.92^\circ$, uppermost mantle seismicity shifts slightly southward with respect to crustal earthquakes, suggesting a change in the fault geometry from west to east (Kuna *et al.* 2019). This may have resulted in the obstruction of fluid transmission pathways, leading to slightly reduced extent of hydrothermal circulation in the easternmost region imaged as relatively faster velocities.

Seismic swarms dominate the uppermost mantle beneath BR (Kuna *et al.* 2019), especially around the central areas where the seismic velocities are relatively slower compared to easternmost region (Figs 6c–f, 9c–f and 11h). Based on identical hypocentre migration rates of creep-triggered swarms in OTFs and continental strike-slip environments where seismic swarms have been associated with geodetically observed creep (Lohman & McGuire 2007), Kuna *et al.* (2019) inferred the uppermost mantle swarms in the BR to be a direct response to aseismic creep caused by the serpentinization of peridotite. In Layer A of our shear-wave tomographic model where the swarms are concentrated, the relatively slow shear-wave velocities ($\sim 4.3\text{--}4.4$ km/s) along most areas in the BR are consistent with serpentinization of up to $\sim 13\text{--}25$ per cent. This corresponds

to a relatively high water content (~ 2.7 wt per cent) some of which may have reached Layer B. The serpentinization of the uppermost mantle is well known to result in a change of its rheology from velocity-weakening to velocity-strengthening frictional behaviour that limits earthquake nucleation and promote aseismic creep. Thus, our tomographic results advocate for extensive uppermost mantle serpentinization beneath the BR, especially within the western to central region, which can explain the documented mantle earthquake swarms in this fault segment (Kuna *et al.* 2019). At uppermost mantle depths, similar slow shear-wave velocities (~ 4.45 km/s) are observed in the easternmost BR and GD (Figs 9c–f), suggesting a similar extent of fluid infiltration that is consistent with the observation of deep seismicity ($\sim 11\text{--}15$ km) in both segments (Kuna 2020; Ren *et al.* 2023).

5.4.3 Cascadia depression

In the centrally located CD, slow shear-wave velocities in the uppermost crust ($\sim 3.4\text{--}3.6$ km/s; Fig. 10a) can be explained by fluid-filled porosity of ~ 2 per cent, indicating relatively strong crustal hydrothermal circulation. Just as in western BTFZ with a similar uppermost crustal structure, here, Kuna (2020) located mostly small magnitude earthquakes ($b=1.36\pm.09$; highest of all segments along Blanco) but reaching depths of ~ 15 km. The relatively faster shear-wave velocities ($\sim 4.45\text{--}4.5$ km/s) in Layer A beneath the CD (Figs 10a and 11h) can be explained by $\sim 1.2\text{--}7$ vol per cent (upto 0.75 wt per cent) serpentinization suggest an uppermost mantle with sparse fluid content compared to the adjacent western part of the BR where ~ 25 vol per cent serpentinization has been inferred. Although this may sufficiently explain the deep earthquakes in the CD, Kuna (2020) suggested quickly cooled sporadic vertical dike intrusions as an alternative explanation. This scenario seems reasonable considering our interpretation of a potential deep magma source beneath the depression in Section 5.3. We, thus, speculate that possible interactions between seawater penetrating Layer A and the intermittent magmatic intrusions may have slightly cooled the segment and increased the velocity in the CD relative to the adjacent western BR. Such deep seismicity that extends into the uppermost mantle has also been reported at ITSCs of the Quebrada transform fault in the EPR (Gong *et al.* 2022).

In summary, there is a relatively strong relationship between structural variations and earthquake behaviour along the BTFZ. The slow seismic velocities (reduced by at least $\sim 4\text{--}8$ per cent relative to the surrounding normal oceanic lithospheres) along the strike of the BTFZ extend virtually from the crust down to depths of ~ 22 km. Their broad interpretations as due to active fracturing that results in $\sim 0.14\text{--}10.9$ per cent fluid-filled porosity and possibly a small component of mineral alteration in the crust, $\sim 1.2\text{--}37$ vol per cent (0.13–4.0 wt per cent) degree of serpentinization and deformation of the uppermost mantle in Layer A, and $\sim >9$ per cent of mantle hydration and/or the presence of $\sim 0.43\text{--}1.6$ per cent melt in Layer B, provide ample evidence for widespread and deep fluid infiltration, occasionally exceeding ~ 15 km depth. Based on current oceanic models that restrict the depth extent of hydrothermal circulation to the maximum depth of seismicity, Kuna (2020) inferred a relatively simple pattern of hydrothermal circulation along the BTFZ. In the western segments that lack deep and large magnitude earthquakes, shallow extent of hydrothermal circulation was suggested. In contrast, in central and eastern Blanco that host relatively large (up to Mw 6.5 along BR) and deep ($\sim 11\text{--}15$ km, especially beneath CD and BR) earthquakes, deeper reach of hydrothermal circulation was

inferred. In a broad sense, our tomographic results and interpretations reflect this pattern but appear to indicate a more complex and nuanced variation, especially along eastern Blanco. Microstructural analysis of altered peridotite mylonites recovered from Shaka and Prince Edwards OTFs in the southwest Indian ridge (Kohli & Warren 2020; Prigent *et al.* 2020) indicate seawater-derived fluid percolate deep into uppermost mantle depths that correspond to $\sim > 850^\circ\text{C}$ isotherm. Also, fairly recent local high-resolution seismicity studies along global OTFs (e.g. McGuire *et al.* 2012; Yu *et al.* 2021; Gong *et al.* 2022) have consistently located earthquakes at depths deeper than ~ 10 km and/or the $\sim 600^\circ\text{C}$ thermal limit on seismic slip (Abercrombie & Ekström 2001; McKenzie *et al.* 2005), suggesting that deep fluid infiltration along OTFs may be a global phenomenon. The only 3-D surface-wave derived shear-wave velocity model over an OTF we could find where deep seismicity have been reported (the Chain TF in the mid-Atlantic) just like the BTFZ, also imaged patches of slow velocities that suggest increased hydrothermal circulation that extend to deeper depths, possibly cooling regions beneath flower structures (Leptokaropoulos *et al.* 2023).

6 CONCLUSION

In this study, we collected and analyzed seismic ambient noise data recorded by 67 OBSs deployed in and around the BTFZ. By removing the coherent pressure signal from the vertical channels prior to cross-correlation, we are able to recover relatively strong first-overtone Rayleigh-wave signals in the period band 3 to 11 s which are sensitive to the crust and uppermost mantle. With the first-overtone Rayleigh-waves, we compute reliable phase velocity dispersion curves and perform tomographic inversion to obtain 2-D phase velocity maps at eleven periods between 4.0 and 8.0 s. Local phase velocity dispersion curves extracted from the phase velocity maps were inverted for 1-D isotropic shear-wave velocity structures using a linearized iterative inversion scheme. They are compiled into a 3-D shear-wave velocity model of the study area, down to a depth of ~ 22 km. In general, both tomographic models (first-overtone Rayleigh-wave phase velocity and shear-wave velocity models) which are rare along global OTFs, especially in the crust and uppermost mantle depths exceeding ~ 15 km, have resulted in the following key findings:

(i) Slow velocities relative to the bounding oceanic plates ($\sim 4\text{--}8$ per cent reduction) are observed at several segments along the BTFZ in the crust but mostly at uppermost mantle depths, exceeding ~ 20 km. Their interpretations as due to intense fracturing in the crust explained by $\sim 0.4\text{--}10.9$ per cent fluid-filled porosity, deformation and $\sim 1.2\text{--}37$ vol per cent (0.13–4.0 wt per cent) degree of serpentinization in Layer A (6–16 km) and $\sim > 9$ per cent mantle hydration and/or the presence of $\sim 0.43\text{--}1.6$ per cent melt in Layer B (> 16 km), provide strong evidence for deep ($\sim > 15$ km) and relatively variable hydrothermal circulation along the BTFZ.

(ii) The along-strike and depth variations in seismic velocities within the seismogenic zone indicate important variations in fault zone material properties that affect the seismic behaviour of the transform fault. Specifically, in the BR where our tomography results suggest deeper extent of hydrothermal circulation and higher degree of uppermost mantle serpentinization (up to ~ 25 per cent) relative to other segments, the change in rheology of the uppermost mantle from velocity-weakening to velocity-strengthening frictional behaviour that has long been associated with widespread

serpentinization may explain the dominance of aseismic slip accompanied by seismic swarms at depths $\sim \geq 8$ km (b-value = 1.13; Kuna *et al.* 2019).

(iii) Low seismic velocities in Layer B within the vicinities of the RTIs explained by the presence of up to ~ 1.6 per cent partial melt support our interpretation of intra-transform magmatism that is potentially facilitated by water-induced melting.

ACKNOWLEDGEMENTS

This work is supported by the National Natural Science Foundation of China (grant 42122060), the Hong Kong Research Grant Council Early Career Scheme (grant 24305521), and the Croucher Tak Wah Mak Innovation Award. The authors acknowledge the constructive comments and suggestions provided by the editor and two anonymous reviewers that have greatly improved the manuscript. We appreciate Satish C. Singh and Zhikai Wang for their assistance in the estimation of mantle hydration and mylonitization. We also thank Haiying Gao for sharing her shear-wave velocity model of the Cascadia subduction system with us. We appreciate Václav M. Kuna for sharing his seismicity catalogue with us.

SUPPORTING INFORMATION

Supplementary data are available at [GJI](#) online.

Figure S1: Bathymetry and fault-plane solutions of ten main earthquake along the BTFZ showing normal (in CD and SD) and strike-slip motions (e.g. BR) obtained from Braunmiller & Nábělek (2008). From the WBD to the GT, the earthquakes include Mw4.7 11/10/1997, Mw5.8 03/11/1981, Mw5.5 12/02/1990, Mw5.0 25/05/1995, Mw4.5 25/09/1995, Mw4.8 04/01/1998, Mw6.4 28/07/1977, Mw6.5 13/03/1985, Mw6.3 27/10/1994 and Mw4.3 22/02/1995. The size of the beach balls indicate the earthquake magnitude. The different segments of the BTFZ shown include WBD: Western Blanco Depression, EBD: Eastern Blanco Depression, SD: Surveyor Depression, CD: Cascadia Depression, BR: Blanco Ridge, and GT: Gorda Transform.

Figure S2: An examples of tilt and compliance noise correction for one month (26/11/2012 - 26/12/2012) of continuous noise data recorded by seismic broadband station BB070 (Fig. 1 in the main text). (a), (b) and (c) are the pressure record, raw and corrected vertical noise data, respectively. (d) shows the power spectra density (PSD) functions of the raw and corrected vertical component records.

Figure S3: Examples of interstation phase velocity estimation using the cross-spectra waveform fitting technique for four station pairs with a wide range of interstation distances and SNRs. Top panels: interstation cross-correlation function with the vertical blue lines marking the 2.0 km/s group velocity. Middle panels: Bessel function fitting where the red and black curves indicate the Bessel function and real part of the CCF, respectively. Bottom panels: Dispersion measurement with the red and grey lines indicating the extracted and starting phase velocities, respectively. The vertical green lines indicate the period band of 3.5 and 8.7 s where measurements are reliable.

Figure S4: (a) and (b), suites of dispersion curves sampling strictly the BTFZ and the entire study region, respectively. The vertical black broken lines indicate period band of 4.0 and 8.0 s.

Figure S5: Examples of final histograms of misfit at selected periods: observed Rayleigh wave phase times minus predictions from the estimated phase velocity tomographic maps using straight ray

theory. The standard deviation of each misfit distribution is presented in each panel.

Figure S6: Phase velocity tomographic maps at 11 distinct time periods. The solid black lines outline the approximate location of the BTFZ and GR. Peripheral regions with zero raypath coverage are masked out.

Figure S7: Phase velocity tomographic maps at 11 distinct time periods. The solid black lines outline the approximate location of the BTFZ and GR. Peripheral regions with zero raypath coverage are masked out.

Figure S8: Checkerboard resolution test at periods 4.0, 5.0 and 7.9 s, using anomaly sizes $0.25^\circ \times 0.25^\circ$, $0.4^\circ \times 0.4^\circ$, $0.5^\circ \times 0.5^\circ$, $0.6^\circ \times 0.6^\circ$, $0.7^\circ \times 0.7^\circ$, $0.9^\circ \times 0.9^\circ$ and $1.0^\circ \times 1.0^\circ$. The recovered patterns are shown.

Figure S9.1: Resolution testing for slow-velocity BTFZ. (a) The input velocity model represented by -5 per cent velocity perturbation from the background phase velocity of 3 km/s. (b)-(g) Recovered models at six distinct selected time periods.

Figure S9.2: Same as Fig. S6.1 but input velocity model is represented by -8 per cent velocity perturbation from the background phase velocity of 3 km/s.

Figure S9.3: Same as Fig. S6.1 but input velocity model is represented by -10 per cent velocity perturbation from the background phase velocity of 3 km/s.

Figure S10: One standard deviation of the population of final Vs model for depth slices shown in the main text. Due to the systematic enforcement of smoothing and damping, uncertainties are slightly lower in regions where ray coverage is minimum, especially at depths > 10 km.

Figure S11: Path coverage at six selected time periods. The line colours indicate the average path phase velocity. The solid black lines show the approximate outline of the BTFZ.

Figure S12: Horizontal slices from the 3-D shear-wave velocity model.

Table S1: Seismic broad-band stations used in this study.

Table S2: Summary of elastic properties of minerals used for the estimation of degree of hydration and fraction of partial melt in uppermost mantle Layer B.

Please note: Oxford University Press is not responsible for the content or functionality of any supporting materials supplied by the authors. Any queries (other than missing material) should be directed to the corresponding author for the paper.

DATA AVAILABILITY

The continuous seismic data underlying this paper are available in the Data Management Center of the Incorporated Research Institutions for Seismology (<https://ds.iris.edu/ds/nodes/dmc/>). Other derived data like the phase velocity dispersion measurements and seismic velocity models can be obtained upon direct request to NIA.

REFERENCES

- Abercrombie, R.E. & Ekström, G., 2001. Earthquake slip on oceanic transform faults, *Nature*, **410**, 74–77.
- Abers, G.A. & Hacker, B.R., 2016. A Matlab toolbox and excel workbook for calculating the densities, seismic wave speeds, and major element composition of minerals and rocks at pressure and temperature, *Geochim. Geophys. Geosyst.*, **17**, 616–624.
- Abrams, L.J., 1986. Morphology and crustal structure of the Kane Fracture Zone transverse ridge, *Master's theses*, Open Access, pp. 814.
- Adimah, N.I. & Padhy, S., 2019. Ambient noise Rayleigh wave tomography across the Madagascar Island, *Geophys. J. Int.*, **220**(3), 1657–1676.
- Aki, K., 1957. Space and time spectra of stationary stochastic waves, with special reference to microtremors, *Bull. Earthq. Res. Inst.*, **35**, 415–456.
- Ambos, E.L. & Hussong, D.M., 1986. Oceanographer transform fault structure compared to that of surrounding oceanic crust: results from seismic refraction data analysis, *J. Geodyn.*, **5**, 79–102.
- Bell, S.W., Forsyth, D.W. & Ruan, Y., 2014. Removing noise from the vertical component records of ocean-bottom seismometers: results from year one of the Cascadia initiative, *Bull. seism. Soc. Am.*, **105**(1), 300–313.
- Bell, S.W., Ruan, Y. & Forsyth, D.W., 2016. Ridge asymmetry and deep aqueous alteration at the trench observed from Rayleigh wave tomography of the Juan de Fuca plate, *J. geophys. Res.*, **121**(10), 7298–7321.
- Bensen, G.D., Ritzwoller, M.H., Barmin, M.P., Levshin, A.L., Lin, F., Moschetti, M.P., Shapiro, N.M. & Yang, Y., 2007. Processing seismic ambient noise data to obtain reliable broad-band surface wave dispersion measurements, *Geophys. J. Int.*, **169**(3), 1239–1260.
- Berryman, J.G., 1992. Single-scattering approximations for coefficients in Biot's equations of poroelasticity, *J. acoust. Soc. Am.*, **91**, 551–571.
- Bickert, M., et al., 2023. Fluid-assisted grain size reduction leads to strain localization in oceanic transform faults, *Nat. Commun.*, **14**, doi:10.1038/s41467-023-39556-5.
- Bird, P., Kagan, Y.Y. & Jackson, D.D., 2002. Plate tectonics and earthquake potential of spreading ridges and oceanic transform faults, in plate boundary zones, *Geodyn. Ser.*, **30**, 201–218.
- Boettcher, M.S. & McGuire, J.J., 2009. Scaling relations for seismic cycles on mid-ocean ridge transform faults, *Geophys. Res. Lett.*, **36**(21), doi:10.1029/2009GL040115.
- Bonatti, E., 1976. Serpentinite intrusions in the oceanic crust, *Earth planet. Sci. Lett.*, **32**, 107–113.
- Bonatti, E., 1978. Vertical tectonism in oceanic fracture zones, *Earth planet. Sci. Lett.*, **37**(3), 369–379.
- Bonte, P., Labeyrie, L., Dudley, W., Blanc, P., Berthois, L., Hékinian, R. & Duplessy, J., 1982. Morphology and tectonics of the Romanche transform-fault high-resolution mapping and precision sampling of the northern slope, *Oceanol. Acta*, **5**(2), 235–240.
- Bowden, D.C., Kohler, M.D., Tsai, V.C. & Weeraratne, D.S., 2016. Offshore southern California lithospheric velocity structure from noise cross-correlation functions, *J. geophys. Res.*, **121**(5), 3415–3427.
- Braunmiller, J. & Nábělek, J., 2008. Segmentation of the Blanco transform fault zone from earthquake analysis: complex tectonics of an oceanic transform fault, *J. geophys. Res.*, **113**(B7), doi:10.1029/2007JB005213.
- Brocher, T., 2005. Empirical relations between elastic wavespeeds and density in the earth's crust, *Bull. seism. Soc. Am.*, **95**(5), 081–2092.
- Bromiley, G.D. & Pawley, A.R., 2003. The stability of antigorite in the systems $\text{mgo-sio}_2\text{-h}_2\text{o}$ (msh) and $\text{mgo-al}_2\text{o}_3\text{-sio}_2\text{-h}_2\text{o}$ (mash): The effects of al^{3+} substitution on high-pressure stability, *Am. Mineral.*, **88**, 99–108.
- Burgos, G., Montagner, J.-P., Beucler, E., Capdeville, Y., Mocquet, A. & Drilleau, M., 2014. Oceanic lithosphere–asthenosphere boundary from surface wave dispersion data, *J. geophys. Res.*, **119**(2), 1079–1093.
- Byrnes, J.S., Toomey, D.R., Hooft, E.E.E., Nábělek, J. & Braunmiller, J., 2017. Mantle dynamics beneath the discrete and diffuse plate boundaries of the Juan de Fuca plate: Results from Cascadia Initiative body wave tomography, *Geochim. Geophys. Geosyst.*, **18**(8), 2906–2929.
- Caine, J., Evans, J. & Forster, C., 1996. Fault zone architecture and permeability structure, *Geology*, **24**, 1025–1028.
- Calvert, A.J. & Potts, C., 1985. Seismic evidence for hydrothermally altered mantle beneath old crust in the Tydeman Fracture Zone, *Earth planet. Sci. Lett.*, **75**(4), 439–449.
- Calvert, A.J., Hasselgren, E.A. & Clowes, R.M., 1990. Oceanic rift propagation—a cause of crustal underplating, and seamount volcanism, *Geology*, **18**(9), 886–889.
- Carlson, R.L. & Miller, D.J., 2004. Influence of pressure and mineralogy on seismic velocities in oceanic gabbros: implications for the composition and state of the lower oceanic crust, *J. geophys. Res.*, **109**(B9), doi:10.1029/2003JB002699.

- Chester, F.M.**, Evans, J.P. & Biegel, R.L., 1993. Internal structure and weakening mechanisms of the San Andreas Fault, *J. geophys. Res.*, **98**(B1), 771–786.
- Cipriani, A.** *et al.*, 2009. A 19 to 17 ma amagmatic extension event at the mid-atlantic ridge: ultramafic mylonites from the vema lithospheric section, *Geochem. Geophys. Geosyst.*, **10**(10), doi:10.1029/2009GC002534.
- Clague, D.**, Paduan, J., Caress, D., McClain, J. & Zierenberg, R., 2020. Lava flows erupted in 1996 on north gorda ridge segment and the geology of the nearby sea cliff hydrothermal vent field from 1-m resolution auv mapping, *Front. Mar. Sci.*, 7–27, doi:10.3389/fmars.2020.00027.
- Clark, A.N.**, Lesser, C.E., Jacobsen, S.D. & Wang, Y., 2016. Anomalous density and elastic properties of basalt at high pressure: reevaluating of the effect of melt fraction on seismic velocity in the earth's crust and upper mantle, *J. geophys. Res.*, **121**(6), 4232–4248.
- Collins, J.A.**, Brocher, T.M. & Purdy, G.M., 1989. Seismic velocity structure at deep sea drilling project site 504b: evidence for thin oceanic crust, *J. geophys. Res.*, **94**, 9283–9302.
- Cox, S.**, Ikari, M.J., MacLeod, C.J. & Fagereng, K., 2021. Frictional characteristics of oceanic transform faults: Progressive deformation and alteration controls seismic style, *Geophys. Res. Lett.*, **48**(24), e2021GL096292, doi:10.1029/2021 GL096292.
- Crawford, W.C.** & Webb, S.C., 2000. Identifying and removing tilt noise from low-frequency (<0.1 Hz) seafloor vertical seismic data, *Bull. seism. Soc. Am.*, **90**(4), 952–963.
- Detrick, R.S.**, Cormier, M.H., Prince, R.A., Forsyth, D.W. & Ambos, E.L., 1982. Seismic constraints on the crustal structure within the Vema Fracture Zone, *J. geophys. Res.*, **87**(B13), 10599–10612.
- Detrick, R.S.**, White, R.S. & Purdy, G.M., 1993. Crustal structure of North Atlantic Fracture Zones, *Rev. Geophys.*, **31**(4), 439–458.
- Divins, D.L.**, 2003. Total Sediment Thickness of the World's Oceans & Marginal Seas, NOAA National Geophysical Data Center, Boulder, CO.
- Drury, M.R.**, Vissers, R.L., der Wal, D.V. & Strating, E.H., 1991. Shear localization in upper mantle peridotites, *Pure appl. Geophys.*, **137**, 439–460.
- Duncan, J.**, 1968. Late pleistocene and postglacial sedimentation and stratigraphy of deep-sea environments off Oregon, Unpublished PhD dissertation, Oregon State University, 222pp.
- Dziak, R.P.**, Fox, C.G. & Embley, R.W., 1991. Relationship between the seismicity and geologic structure of the Blanco transform fault zone, *Mar. Geophys. Res.*, **13**, 203–208.
- Dziak, R.P.**, Fox, C., Embley, R., Nábělek, J., Braunmiller, J. & Koski, R., 2000. Recent tectonics of the Blanco ridge, eastern Blanco transform fault zone, *Mar. Geophys. Res.*, **21**(5), 423–450.
- Eakin, C.M.**, Rychert, C.A. & Harmon, N., 2018. The role of oceanic transform faults in seafloor spreading: a global perspective from seismic anisotropy, *J. geophys. Res.*, **123**(2), 1736–1751.
- Embley, R.W.** & Wilson, D., 1992. Morphology of the Blanco Transform Fault Zone-NE Pacific: implications for its tectonic evolution, *Mar. geophys. Res.*, **14**, 25–45.
- Engeln, J.F.**, Wiens, D.A. & Stein, S., 1986. Mechanisms and depths of Atlantic transform earthquakes, *J. geophys. Res.*, **91**(B1), 548–577.
- Eshelby, J.**, 1957. The determination of the elastic field of an ellipsoidal inclusion, and related problems, *Proc. R. Soc. Lond.*, **A241**, 376–396.
- Evans, B.W.**, 2004. The serpentinite multisystem revisited: chrysotile is metastable, *Inter. Geol. Rev.*, **46**, 479–506.
- Faulkner, D.**, Jackson, C., Lunn, R., Schlische, R., Shipton, Z., Wibberley, C. & Withjack, M., 2010. A review of recent developments concerning the structure, mechanics and fluid flow properties of fault zones, *J. Struct. Geol.*, **32**, 1557–1575.
- Faulkner, D.R.**, Lewis, A.C. & Rutter, E.H., 2003. On the internal structure and mechanics of large strike-slip fault zones: field observations of the carboneras fault in southeastern spain, *Tectonophysics*, **367**(3–4), 235–251.
- Feng, L.** & Ritzwoller, M.H., 2019. A 3-D shear velocity model of the crust and uppermost mantle beneath Alaska including apparent radial anisotropy, *J. geophys. Res.: Solid Earth*, **124**(10), 10468–10497.
- Fornari, D.J.**, Gallo, D.G., Edwards, M.H., Madsen, J.A., Perfit, M.R. & Shor, A.N., 1989. Structure and topography of the Siqueiros Transform Fault System: evidence for the development of intra-transform spreading centers, *Mar. Geophys. Res.*, **11**, 263–299.
- Fox, P.J.** & Gallo, D.G., 1984. A tectonic model for ridge-transform-ridge plate boundaries: implications for the structure of oceanic lithosphere, *Tectonophysics*, **104**(3), 205–242.
- Gaetani, G.A.**, DeLong, S.E. & Wark, D.A., 1995. Petrogenesis of basalts from the Blanco trough, northeast pacific: Inferences for off-axis melt generation, *J. geophys. Res.*, **100**(B3), 4197–4214.
- Gallo, D.**, Fox, P.J. & Macdonald, K.C., 1986. A seabeam investigation of the Clipperton transform fault: the morphotectonic expression of a fast-slipping transform boundary, *J. Geophys. Res.*, **91**, 3455–3467.
- Gallo, D.**, Fornari, D.J., Madsen, J., Perfit, M.R. & Shor, A.N., 1987. Sea MARC II survey of the siqueiros transform, *EOS, Trans. Am. geophys. Un.*, **68**, 1505, doi:10.1007/BF00282579.
- Gallo, D.**, Fox, P. & Macdonald, K., 2012. A sea beam investigation of the Clipperton Transform Fault: the morphotectonic expression of a fast-slipping transform boundary, *J. geophys. Res.*, **91**(B3), 3455–3467.
- Gao, H.**, 2016. Seismic velocity structure of the Juan de Fuca and Gorda plates revealed by a joint inversion of ambient noise and regional earthquakes, *Geophys. Res. Lett.*, **43**(10), 5194–5201.
- Gao, H.**, 2018. Three-dimensional variations of the slab geometry correlate with earthquake distributions at the Cascadia subduction system, *Nat. Commun.*, **9**, 1204, doi:10.1038/s41467-018-03655-5.
- Gao, H.** & Shen, Y., 2015. A preliminary full-wave ambient-noise tomography model spanning from the Juan de Fuca and Gorda Spreading Centers to the Cascadia volcanic arc, *Seismol. Res. Lett.*, **86**(5), 1253–1260.
- Godfrey, K.E.**, Dalton, C.A., Ma, Z., Hjörleifsdóttir, V. & Ekström, G., 2019. A comparison of approaches for the prediction and inversion of surface wave phase delays, *Geophys. J. Int.*, **217**(3), 1496–1514.
- Goff, J.**, Fornari, D., Cochran, J., Keeley, C. & Malinverno, A., 1993. Wilkes transform system and “nannopllate”, *Geology*, **21**(7), 623–626.
- Gong, J.** & Fan, W., 2022. Seismicity, fault architecture, and slip mode of the westernmost gofar transform fault, *J. geophys. Res.*, **127**(11), e2022JB024918, doi:10.1029/2022JB024918.
- Gong, J.**, Fan, W. & Parnell-Turner, R., 2022. Microseismicity indicates atypical small-scale plate rotation at the quebrada transform fault system, east pacific rise, *Geophys. Res. Lett.*, **49**(3), e2021GL097000, doi:10.1029/2021GL097000.
- Gong, J.**, Fan, W. & Parnell-Turner, R., 2023. Machine learning-based new earthquake catalog illuminates on-fault and off-fault seismicity patterns at the discovery transform fault, east Pacific rise, *Geochim. Geophys. Geosyst.*, **24**(9), e2023GC011043, doi:10.1029/2023GC011043.
- Goutorbe, B.**, de Oliveira Coelho, D.L. & Drouet, S., 2015. Rayleigh wave group velocities at periods of 6–23 s across Brazil from ambient noise tomography, *Geophys. J. Int.*, **203**(2), 869–882.
- Gregg, P.M.**, Lin, J., Behn, M.D. & Montesi, L.G.J., 2007. Spreading rate dependence of gravity anomalies along oceanic transform faults, *Nature*, **448**, 183–187.
- Gregory, E.P.**, Singh, S.C., Marjanović, M. & Wang, Z., 2021. Serpentinized peridotite versus thick mafic crust at the Romanche oceanic transform fault, *Geology*, **49**(9), 1132–1136.
- Grevemeyer, I.**, Rüpke, L., Morgan, J., Karthik, I. & Colin, W., 2021. Extensional tectonics and two-stage crustal accretion at oceanic transform faults, *Nature*, **591**, 402–407.
- Grove, K.** *et al.*, 2021. Seismic structure of the St. Paul Fracture Zone and late cretaceous to mid eocene oceanic crust in the equatorial atlantic ocean near 18°W, *J. geophys. Res.*, **126**(11), e2021JB022456, doi:10.1029/2021JB022456.
- Gualtieri, L.**, Stutzmann, E., Capdeville, Y., Farra, V., Mangeney, A. & Morelli, A., 2015. On the shaping factors of the secondary microseismic wavefield, *J. geophys. Res.*, **120**(9), 6241–6262.
- Harmon, N.**, Rychert, C.A., Kendall, J.M., Agius, M., Bogiatzis, P. & Tharimena, S., 2020. Evolution of the oceanic lithosphere in the equatorial Atlantic from Rayleigh wave tomography, evidence for small-scale convection from the pi-lab experiment, *Geochim. Geophys. Geosyst.*, **21**(9), e2020GC009174, doi:10.1029/2020GC009174.

- Hart, R.**, Pyle, D. & Robbins, J., 1986. Hydrothermal sulphides, breccias and greenstones from the gorda depression, Oregon Dept. Mines and Mineral Resources Open File Rept., pp. 86–16.
- Hart, R.**, Hoefs, J. & Pyle, D., 1990. Multistage hydrothermal systems in the Blanco fracture zone, in *Gorda Ridge*, pp. 51–75, Springer, ed. McMurray, G.R., doi:10.1007/978-1-4612-3258-2-4.
- Hashin, Z.** & Shtrikman, S., 1963. A variational approach to the theory of the elastic behaviour of multiphase materials, *J. Mech. Phys. Solids*, **11**(2), 127–140.
- Hensen, C.** et al., 2019. Marine transform faults and fracture zones: a joint perspective integrating seismicity, fluid flow and life, *Front. Earth Sci.*, 7–39.
- Herrmann, R.** & Ammon, C., 2004. Surface waves, receiver functions and crustal structure, Computer Programs in Seismology, Version 3.30. Saint Louis University, Saint Louis.
- Hey, R.N.** & Wilson, D.S., 1982. Propagating rift explanation for the tectonic evolution of the northeast pacific—the pseudomovie, *Earth planet. Sci. Lett.*, **58**, 167–188.
- Hirschmann, M.M.**, 2010. Partial melt in the oceanic low velocity zone, *Phys. Earth planet. Inter.*, **179**, 60–71.
- Ibach, D.H.**, 1981. The structure and tectonics of the Blanco fracture zone, MS thesis, Oreg. State Univ., Corvallis, 60pp.
- Janiszewski, H.A.**, Gaherty, J.B., Abers, G.A., Gao, H. & Eilon, Z.C., 2019. Amphibious surface-wave phase-velocity measurements of the Cascadia subduction zone, *Geophys. J. Int.*, **217**(3), 1929–1948.
- Ji, J.**, 2006. Cgg method for robust inversion and its application to velocity-stack inversion, *Geophysics*, **71**(4), R59–R67.
- Ji, S.**, Li, A., Wang, Q., Long, C., Wang, H., Marcotte, D. & Salisbury, M., 2013. Seismic velocities, anisotropy, and shear-wave splitting of antigorite serpentinites and tectonic implications for subduction zones, *J. geophys. Res.*, **118**, 1015–1037.
- Jiang, C.** & Denolle, M., 2020. Noisepy: A new high-performance python tool for ambient-noise seismology [software], *Seismol. Res. Lett.*, **91**, 1853–1866.
- Karson, J.A.** & Dick, H. J.B., 1983. Tectonics of ridge-transform intersections at the Kane Fracture Zone, *Mar. Geophys. Res.*, **6**, 51–98.
- Karson, J.A.**, Tivey, M.A. & Delaney, J.R., 2002. Internal structure of uppermost oceanic crust along the western Blanco transform scarp: implications for subaxial accretion and deformation at the Juan de Fuca Ridge, *J. geophys. Res.*, **107**(B9), EPM 1–1–EPM 1–24, doi:10.1029/2000JB000051.
- Katz, R.F.**, Spiegelman, M. & Langmuir, C.H., 2003. A new parameterization of hydrous mantle melting, *Geochem. Geophys. Geosyst.*, **4**, 1073, doi:10.1016/0020-7683(66)90002-3.
- Keller, T.** & Katz, R.F., 2016. The role of volatiles in reactive melt transport in the asthenosphere, *J. Petrol.*, **57**, 1073–1108.
- Kohli, A.H.** & Warren, J.M., 2020. Evidence for a deep hydrologic cycle on oceanic transform faults, *J. geophys. Res.*, **125**(2), e2019JB017751, doi:10.1029/2019JB017751.
- Kuna, V.**, 2020. *Investigation of Slip and Tectonics of the Blanco Transform Fault using High-Resolution Ocean Bottom Seismic Data*, PhD thesis, Oregon State University.
- Kuna, V.**, Nabelek, J. & Braunmiller, J., 2019. Mode of slip and crust–mantle interaction at oceanic transform faults., *Nat. Geosci.*, **12**, 138–142.
- Kuster, G.T.** & Toksöz, M.N., 1974. Velocity and attenuation of seismic waves in two-phase media; part i, theoretical formulations, *Geophysics*, **39**(5), 587–606.
- Leptokaropoulos, K.**, Rychert, C., Harmon, N., Schlaphorst, D., Grevenmeyer, I., Kendall, J. & Singh, S.C., 2023. Broad fault zones enable deep fluid transport and limit earthquake magnitudes, *Nat. Commun.*, **14**, 5748.
- Lin, F.-C.**, Ritzwoller, M.H. & Snieder, R., 2009. Eikonal tomography: surface wave tomography by phase front tracking across a regional broadband seismic array, *Geophys. J. Int.*, **177**(3), 1091–1110.
- Lohman, R.B.** & McGuire, J.J., 2007. Earthquake swarms driven by aseismic creep in the Salton trough, California, *J. geophys. Res.*, **112**(B4), doi:10.1029/2006JB004596.
- Luo, Y.**, Xia, J., Miller, R., Xu, Y., Liu, J. & Liu, Q., 2008. Rayleigh-wave dispersive energy imaging using a high-resolution linear radon transform, *Pure appl. Geophys.*, **165**(5), 903–922.
- Luo, Y.**, Xia, J., Miller, R., Xu, Y., Liu, J. & Liu, Q., 2009. Rayleigh-wave mode separation by high-resolution linear radon transform, *Geophys. J. Int.*, **179**(1), 254–264.
- Luo, Y.**, Xu, Y. & Yang, Y., 2012. Crustal structure beneath the dabie orogenic belt from ambient noise tomography, *Earth planet. Sci. Lett.*, **313–314**, 12–22.
- Luo, Y.**, Yang, Y., Zhao, K., Xu, Y. & Xia, J., 2015. Unraveling overtone interferences in love-wave phase velocity measurements by radon transform, *Geophys. J. Int.*, **203**(1), 327–333.
- Luo, Y.**, Lin, J., Yang, Y., Wang, L., Yang, X. & Xie, J., 2018. Joint inversion of active sources and ambient noise for near-surface structures: a case study in the Balikun Basin, China, *Seismol. Res. Lett.*, **89**(6), 2256–2265.
- Maia, M.**, Sichel, S., Briais, A., Brunelli, D., Ligi, M., Ferreira, N. et al., 2016. Extreme mantle uplift and exhumation along a transpressive transform fault, *Nat. Geosci.*, **9**(8), 619–623.
- Marjanović, M.**, Carbotte, S.M., Nedimović, M.R. & Canales, J.P., 2011. Gravity and seismic study of crustal structure along the Juan de Fuca ridge axis and across pseudofaults on the ridge flanks, *Geochem. Geophys. Geosyst.*, **12**(5), doi:10.1029/2010GC003439.
- McGuire, J.J.**, Ihmlé, P. & Jordan, T., 1996. Time-domain observations of a slow precursor to the 1994 Romanche transform earthquake, *Science*, **274**, 82–85.
- McGuire, J.J.**, Collins, J.A., Gouédard, P., Roland, E., Lizarralde, D., Boettcher, M.S. & van der Hilst, R.D., 2012. Variations in earthquake rupture properties along the Gofar Transform Fault, East Pacific Rise, *Nat. Geosci.*, **5**(5), 336–341.
- McKenzie, D.**, Jackson, J. & Priestley, K., 2005. Thermal structure of oceanic and continental lithosphere, *Earth planet. Sci. Lett.*, **233**(3), 337–349.
- McManus, D.A.**, 1967. Blanco fracture zone, northeast pacific ocean, *Mar. Geol.*, **3**, 429–455.
- Mehouachi, F.** & Singh, S.C., 2018. Water-rich sublithospheric melt channel in the equatorial Atlantic Ocean, *Nat. Geosci.*, **11**, 65–69.
- Melson, W.G.**, 1969. Preliminary Results of a Geophysical Study of Portions of the Juan de Fuca Ridge and Blanco Fracture Zone: A Study Performed Aboard the USC & GS Ship Oceanographer, October 15–26, 1968, Vol. 6 of ESSA technical memorandum C & GSTM, Environmental Science Services Administration (ESSA) Technical Memorandum, U.S. Dept. Commerce, 33pp.
- Menard, H.W.** & Atwater, T., 1968. Changes in direction of sea floor spreading, *Nature*, **219**, 463–467.
- Menke, W.**, 2012. *Geophysical Data Analysis: Discrete Inverse Theory*, 3rd edn, Academic Press.
- Menke, W.** & Jin, G., 2015. Waveform fitting of cross spectra to determine phase velocity using AKI's formula, *Bull. seism. Soc. Am.*, **105**(3), 1619–1627.
- Muller, M.R.**, Minshull, T.A. & White, R.S., 2000. Crustal structure of the southwest Indian Ridge at the Atlantis II Fracture Zone, *J. geophys. Res.*, **105**(B11), 25 809–25 828.
- Nabelek, J.** & Braunmiller, J., 2012. Plate boundary evolution and physics at an oceanic transform fault system [dataset], International Federation of Digital Seismograph Networks, doi:10.7914/SN/X9_2012.
- Nabelek, J.** & Braunmiller, J., 2013. Seismicity, structure and dynamics of the gorda deformation zone [dataset], International Federation of Digital Seismograph Networks, doi:10.7914/SN/Z5_2013.
- Nedimović, M.R.**, Carbotte, S.M., Diebold, J.B., Harding, A.J., Canales, J.P. & Kent, G.M., 2008. Upper crustal evolution across the Juan de Fuca Ridge flanks, *Geochem. Geophys. Geosyst.*, **9**(9), doi:10.1029/2008GC002085.
- Nur, A.** & Simmons, G., 1969. The effect of viscosity of a fluid phase on velocity in low porosity rocks, *Earth planet. Sci. Lett.*, **7**, 99, doi:10.1016/0012-821X(69)90021-1.
- Okazaki, K.**, Burdette, E. & Hirth, G., 2021. Rheology of the fluid oversaturated fault zones at the brittle-plastic transition, *J. geophys. Res.*, **126**(2), e2020JB020804, doi:10.1029/2020JB020804.
- Perfit, M.** et al., 1996. Recent volcanism in the siqueiros transform fault: picritic basalts and implications for Morb magma genesis, *Earth planet. Sci. Lett.*, **141**(1), 91–108.

- Pockalny, R.A., Detrick, R.S. & Paul J. Fox, P.J., 1988. Morphology and tectonics of the Kane transform from sea beam bathymetry data, *J. geophys. Res.*, **93**, 3179–3193.
- Pockalny, R.A., Fox, P.J., Fornari, D.J., Macdonald, K.C. & Perfit, M.R., 1997. Tectonic reconstruction of the clipperton and siqueiros fracture zones: evidence and consequences of plate motion change for the last 3 Myr, *J. geophys. Res.*, **102**(B2), 3167–3181.
- Porritt, R.W., Allen, R.M., Boyarko, D.C. & Brudzinski, M.R., 2011. Investigation of Cascadia segmentation with ambient noise tomography, *Earth planet. Sci. Lett.*, **309**(1), 67–76.
- Prigent, C., Warren, J., Kohli, A. & Teyssier, C., 2020. Fracture-mediated deep seawater flow and mantle hydration on oceanic transform faults, *Earth planet. Sci. Lett.*, **532**, 115988, doi:10.1016/j.epsl.2019.115988.
- Rathnayaka, S. & Gao, H., 2017. Crustal-scale seismic structure from trench to forearc in the Cascadia subduction zone, *J. geophys. Res.*, **122**(9), 7311–7328.
- Ren, Y., Lange, D. & Grevemeyer, I., 2023. Seismotectonics of the Blanco transform fault system, Northeast Pacific: evidence for an immature plate boundary, *J. geophys. Res.*, **128**(3), e2022JB026045, doi:10.1029/2022JB026045.
- Roland, E., Behn, M.D. & Hirth, G., 2010. Thermal-mechanical behavior of oceanic transform faults: implications for the spatial distribution of seismicity, *Geochem. Geophys. Geosyst.*, **11**(7), doi:10.1029/2010GC003034.
- Roland, E., Lizarralde, D., McGuire, J.J. & Collins, J.A., 2012. Seismic velocity constraints on the material properties that control earthquake behavior at the quebrada-discovery-Gofar Transform Faults, East Pacific Rise, *J. geophys. Res.*, **117**(B11), doi:10.1029/2012JB009422.
- Roux, P., Sabra, K.G., Kuperman, W.A. & Roux, A., 2005. Ambient noise cross correlation in free space: theoretical approach, *J. acoust. Soc. Am.*, **117**(1), 79–84.
- Rüpke, L., Morgan, J., Hort, M. & Connolly, J., 2004. Serpentinite and the subduction zone water cycle, *Earth planet. Sci. Lett.*, **223**, 17–34.
- Russell, J.B., 2021. Structure and evolution of the oceanic lithosphere-asthenosphere system from high-resolution surface-wave imaging, *PhD thesis*, ProQuest Dissertations and Theses, Retrieved from <https://www.proquest.com/dissertations-theses/structure-evolution-oceanic-lithosphere/docview/2492599842/se-2?accountid=14522>.
- Russell, J.B. & Gaherty, J.B., 2021. Lithosphere structure and seismic anisotropy offshore eastern North America: implications for continental breakup and ultra-slow spreading dynamics, *J. geophys. Res.*, **126**(12), e2021JB022955, doi:10.1029/2021JB022955.
- Ryan, W.B. et al., 2009. Global multi-resolution topography synthesis, *Geochem. Geophys. Geosyst.*, **10**(3), doi:10.1029/2008GC002332.
- Sandwell, D., Müller, R., Smith, W., Garcia, E. & Francis, R., 2014. Marine geophysics new global marine gravity model from CryoSat-2 and Jason-1 reveals buried tectonic structure, *Science*, **346**(6205), 65–67.
- Savage, H.M. & Brodsky, E.E., 2011. Collateral damage: evolution with displacement of fracture distribution and secondary fault strands in fault damage zones, *J. geophys. Res.*, **116**(B3), doi:10.1029/2010JB007665.
- Schlaphorst, D., Rychert, C.A., Harmon, N., Hicks, S.P., Bogiatzis, P., Kendall, J.-M. & Abercrombie, R.E., 2023. Local seismicity around the Chain Transform Fault at the Mid-Atlantic Ridge from OBS observations, *Geophys. J. Int.*, **234**(2), 1111–1124.
- Searle, R.C., Thomas, M.V. & Jones, E.J.W., 1994. Morphology and tectonics of the romanche transform and its environs., *Mar. Geophys. Res.*, **16**, 427–453.
- Shapiro, N., Campillo, M., Stehly, L. & Ritzwoller, M., 2005. High-resolution surface wave tomography from ambient seismic noise, *Science*, **307**, 1615–1618.
- Shen, W. et al., 2016. A seismic reference model for the crust and uppermost mantle beneath China from surface wave dispersion, *Geophys. J. Int.*, **206**(2), 954–979.
- Smith, W. & Sandwell, D., 1997. Global sea floor topography from satellite altimetry and ship depth soundings, *Science*, **277**(5334), 1956–1962.
- Stakes, D.S., Perfit, M.R., Tivey, M.A., Caress, D.W., Ramirez, T.M. & Maher, N., 2006. The cleft revealed: geologic, magnetic, and morphologic evidence for construction of upper oceanic crust along the southern Juan de Fuca ridge, *Geochem. Geophys. Geosyst.*, **7**, doi:10.1029/2005GC001038.
- Tartarotti, P., Susini, S., Nimis, P. & Ottolini, L., 2002. Melt migration in the upper mantle along the Romanche fracture zone (equatorial Atlantic), *Lithos*, **63**(3), 125–149.
- Taylor, M. A.J. & Singh, S.C., 2002. Composition and microstructure of magma bodies from effective medium theory., *Geophys. J. Int.*, **149**, 15–21.
- Tpley, F.J., Lundstrom, C.C., Sims, K.W. & Hékinian, R., 2004. U-series disequilibria in Morb from the Garrett transform and implications for mantle melting, *Earth planet. Sci. Lett.*, **223**(1), 79–97.
- Thomas, M.F.H., Heine, C., van Itterbeeck, J., Ostanin, I., Seregin, A., Spaak, M., Morales, T. & Essink, T.O., 2022. A new model for the evolution of oceanic transform faults based on 3D broadband seismic observations from São Tomé and Príncipe in the eastern Gulf of Guinea, *Geochem. Geophys. Geosyst.*, **23**(11), e2022GC010351, doi:10.1029/2022GC010351.
- Thompson, G. & Melson, W.G., 1972. The petrology of oceanic crust across fracture zones in the Atlantic ocean: evidence of a new kind of seafloor spreading, *J. Geol.*, **80**, 526–538.
- Tian, Y. & Ritzwoller, M.H., 2017. Improving ambient noise cross-correlations in the noisy ocean bottom environment of the Juan de Fuca plate, *Geophys. J. Int.*, **210**(3), 1787–1805.
- Tian, Y., Shen, W. & Ritzwoller, M.H., 2013. Crustal and uppermost mantle shear velocity structure adjacent to the Juan de Fuca ridge from ambient seismic noise, *Geochem. Geophys. Geosyst.*, **14**(8), 3221–3233.
- Toomey, D. et al., 2014. The Cascadia initiative: a sea change in seismological studies of subduction zones [dataset], *Oceanography*, **27**, 138–150.
- Tozer, B., Sandwell, D.T., Smith, W.H.F., Olson, C., Beale, J.R. & Wessel, P., 2019. Global bathymetry and topography at 15 arc sec: Srtm15+, *Earth Space Sci.*, **6**(10), 1847–1864.
- Tréhu, A.M. & Purdy, G.M., 1984. Crustal structure in the orozco transform zone, *J. geophys. Res.*, **89**(B3), 1834–1842.
- Van Avendonk, H.J.A., Harding, A.J., Orcutt, J.A. & McClain, J.S., 1998. A two-dimensional tomographic study of the Clipperton transform fault, *J. geophys. Res.*, **103**(B8), 17 885–17 899.
- Van Avendonk, H.J.A., Harding, A.J., Orcutt, J.A. & McClain, J.S., 2001. Contrast in crustal structure across the clipperton transform fault from travel time tomography, *J. geophys. Res.*, **106**(B6), 10 961–10 981.
- VanderBeek, B.P. & Toomey, D.R., 2019. Pn tomography of the Juan de Fuca and Gorda plates: implications for mantle deformation and hydration in the oceanic lithosphere, *J. geophys. Res.*, **124**(8), 8565–8583.
- Vera, E.E., Mutter, J.C., Buhl, P., Orcutt, J.A., Harding, A.J., Kappus, M.E., Detrick, R.S. & Brocher, T.M., 1990. The structure of 0-to 0.2-My-old oceanic crust at 9 n on the east pacific rise from expanded spread profiles, *J. geophys. Res.*, **95**(B10), 15 529–15 556.
- Wagner, L., Forsyth, D.W., Fouch, M.J. & James, D.E., 2010. Detailed three-dimensional shear wave velocity structure of the northwestern united states from Rayleigh wave tomography, *Earth planet. Sci. Lett.*, **299**(3), 273–284.
- Walsh, J.B., 1969. New analysis of attenuation in partially melted rock, *J. geophys. Res.*, **74**, 4333, doi:10.1029/JB074i017p04333.
- Wang, Z., Singh, S., Prigent, C., Gregory, E.P.M. & Marjanović, M., 2022. Deep hydration and lithospheric thinning at oceanic transform plate boundaries, *Nat. Geosci.*, **15**, 741–746.
- Webb, S. & Crawford, W., 1999. Long-period seafloor seismology and deformation under ocean waves, *Bull. seism. Soc. Am.*, **89**(6), 1535–1542.
- Wehner, D., Rawlinson, N., Greenfield, T., Daryono, Miller, M.S., Supendi, P., Lü, C. & Widiyantoro, S., 2022. Sassier22: full-waveform tomography of the eastern Indonesian region that includes topography, bathymetry, and the fluid ocean, *Geochem. Geophys. Geosyst.*, **23**(11), e2022GC010563, doi:10.1029/2022GC010563.
- White, R.S., Detrick, R.S., Sinha, M.C. & Cormier, M.H., 1984. Anomalous seismic crustal structure of oceanic fracture zones, *Geophys. J. Int.*, **79**(3), 779–798.
- Wilson, D., 1993. Confidence intervals for motion and deformation of the Juan de Fuca plate, *J. geophys. Res.*, **98**(B9), 16 053–16 071.

- Wilson, D., Hey, R. & Nishimura, C., 1984. Propagation as a mechanism of reorientation of the Juan de Fuca ridge, *J. geophys. Res.*, **89**, 9215–9225.
- Wilson, J., 1965. A new class of faults and their bearing on continental drift, *Nature*, **207**, 343–347.
- Wolfson-Schwehr, M. & Boettcher, M.S., 2019. Chapter 2 - Global characteristics of oceanic transform fault structure and seismicity, in *Transform Plate Boundaries and Fracture Zones*, pp. 21–59, ed. Duarte, J.C., Elsevier.
- Wolfson-Schwehr, M., Boettcher, M.S., McGuire, J.J. & Collins, J.A., 2014. The relationship between seismicity and fault structure on the discovery transform fault, east Pacific Rise, *Geochem. Geophys. Geosyst.*, **15**(9), 3698–3712.
- Wu, M., Wang, H., Zhang, S. & Ritzwoller, M.H., 2023. Plate age and uppermost mantle structure across the Juan de Fuca and Gorda plates, *J. geophys. Res.*, **128**(8), e2023JB026494, doi:10.1029/2023JB026494.
- Wu, T.T., 1966. The effect of inclusion shape on the elastic moduli of a two-phase material, *Int. J. Solids Struct.*, **2**, 1–8.
- Yang, X., Luo, Y., Xu, H. & Zhao, K., 2020. Shear wave velocity and radial anisotropy structures beneath the central Pacific from surface wave analysis of obs records, *Earth planet. Sci. Lett.*, **534**, 116086, doi:10.1016/j.epsl.2020.
- Yang, Y., Ritzwoller, M.H., Levshin, A.L. & Shapiro, N.M., 2007. Ambient noise Rayleigh wave tomography across Europe, *Geophys. J. Int.*, **168**(1), 259–274.
- Yu, Z., Singh, S.C., Gregory, E.P.M., Maia, M., Wang, Z. & Brunelli, D., 2021. Semibrittle seismic deformation in high-temperature mantle mylonite shear zone along the Romanche transform fault, *Sci. Adv.*, **7**, eabf3388, doi:10.1126/sciadv.abf3388.
- Zhang, S., Wang, H., Wu, M. & Ritzwoller, M.H., 2021. Isotropic and azimuthally anisotropic Rayleigh wave dispersion across the Juan de Fuca and Gorda plates and U.S. Cascadia from earthquake data and ambient noise two- and three-station interferometry, *Geophys. J. Int.*, **226**(2), 862–883.